Localization and dynamic changes of neuregulin-1 at C-type synaptic boutons in association with motor neuron injury and repair

Sara Salvany[1], Anna Casanovas[1], Olga Tarabal[1], Lídia Piedrafita[1], Sara Hernández[1], Manuel Santafé[2], María Clara Soto-Bernardini[3], Jordi Calderó[1], Markus H. Schwab[4, 5,]* Josep E. Esquerda[1,]*

[1]Unitat de Neurobiologia Cel·lular, Departament de Medicina Experimental, Facultat de Medicina, Universitat de Lleida and Institut de Recerca Biomèdica de Lleida (IRBLLEIDA), Lleida, Catalonia, Spain

[2]Unitat d'Histologia i Neurobiologia (UHN), Facultat de Medicina i Ciències de la Salut, Universitat Rovira i Virgili, Reus, Catalonia, Spain.

[3]Instituto Tecnológico de Costa Rica (TEC), Cartago, Costa Rica

[4]Hannover Medical School, Hannover, Germany.

[5]Center for Systems Neuroscience (ZSN), Hannover, Germany

Sara Salvany and Anna Casanovas equally contributed to this work

*Corresponding author: Josep E. Esquerda, Unitat de Neurobiologia Cel·lular, Departament de Medicina Experimental, Facultat de Medicina, IRBLLEIDA, Universitat de Lleida, Av. Rovira Roure 80, 25198 Lleida, Catalonia, Spain. Phone: +34-973-702427. E-mail address: josep.esquerda@mex.udl.cat

*Co-corresponding author: Markus H. Schwab, Hannover Medical School, Hannover, Germany. E-mail address: schwab.markus@mh-hannover.de

Running title: Neuregulin-1 at C-type synapses on motor neurons

Non-standard abbreviations

AChR, acetylcholine receptor

ACSF, artificial cerebrospinal fluid

AHP, afterhyperpolarization

ALS, amyotrophic lateral sclerosis

BACE1, β-site amyloid precursor protein–cleaving enzyme1

BiP, binding immunoglobulin protein

CSF, cerebrospinal fluid

CTB, cholera toxin-B

EGF, epidermal growth factor

EM, electron microscopy

ER, endoplasmic reticulum

HA-NRG1^{FL}, HA-tagged full-length NRG1 type III

HA-NRG1^{GIEF}, HA-tagged NRG1 type III processing by BACE1 cleavage

i.p., intraperitoneally

ICD, intracellular domain

MN, motor neuron

NRG1, neuregulin 1

OCM, oculomotor

PB, phosphate buffer

PFA, paraformaldehyde

Pi-elF2α, phosphorylated-eukaryotic initiation factor 2

PM, plasma membrane

S1R, sigma-1 receptor

SOD1, superoxide dismutase 1

SSC, subsynaptic cistern

TSA, tyramide signal amplification

VAChT, vesicular acetylcholine transporter

VGLUT1, vesicular glutamate transporter 1

WT, wild-type

Abstract

C-type synaptic boutons are cholinergic motor neuron (MN) afferents displaying an endoplasmic reticulum-related subsynaptic cistern (SSC) adjacent to the postsynaptic membrane. A constellation of proteins is clustered at C-boutons, including M2 muscarinic receptors, potassium channels and sigma-1 receptors. We previously found that neuregulin (NRG) 1 is associated with C-boutons at postsynaptic SSCs, whereas its ErbB receptors are located at the presynaptic compartment. C-bouton-mediated regulation of MN excitability has been implicated in MN vulnerability. To address the involvement of C-boutons during pathological conditions, we investigated their plastic changes after electrical stimulation, pharmacological treatments and peripheral nerve axotomy. NRG1 clusters were disrupted in acutely stressed MNs and after tunicamycin-induced ER stress. In axotomized MNs C-bouton loss occurred in concomitance with microglial recruitment and was prevented by the ER-stress inhibitor salubrinal. Activated microglia displayed a positive chemotaxis to C-boutons. Analysis of transgenic mice overexpressing NRG1 type I and type III isoforms revealed that NRG1 type III acts as a specific organizer of SSC-like structures, whereas NRG1 type I promotes cholinergic synaptogenesis. Thus, distinct NRG1 isoform-mediated signaling functions regulate the complex matching between pre- and postsynaptic elements at C-boutons. Overall, these data provide new insights into C-bouton-associated molecules as therapeutic targets in MN disease.

Keywords: spinal cord; motor neuron; C-bouton; neuregulin; nerve transection; microglia

Introduction

Lower motor neurons (MNs) in the ventral spinal cord and brain stem project to skeletal muscles and govern the final efferent pathway that determines motor behavior. To achieve a coordinated control of muscle activity, MNs receive a variety of synaptic inputs, which shape appropriate patterns of discharge of muscle-specific MN pools (1, 2). Among the synaptic afferents involved in the regulation of MN excitability, C-boutons are particularly relevant due to their capacity to modulate the strength of the action potential afterhyperpolarization (AHP) via a reduction of outward K^+ currents (3). C-boutons originate from cholinergic $V0_C$ interneurons located close to the central canal (4) and display a particular postsynaptic morphology with a prominent endoplasmic reticulum (ER)-related subsynaptic cistern (SSC) (3, 5). In addition to M2 muscarinic acetylcholine receptors (AChRs) at the postsynaptic plasma membrane (PM) (6), a specific constellation of signaling proteins in the PM and SSC of C-boutons has been described. These include: the voltage-gated K^+ channel Kv2.1 (7), Ca^{2+} activated K^+ (SK) channels (8), and sigma-1 receptors (S1Rs, (9). Most of these proteins are clustered in non-overlapping microdomains within SSC (10, 11), but their exact roles and functional organization are largely unknown. One novel intriguing aspect of the molecular assembly at C-boutons is the accumulation of neuregulin (NRG) 1 in the SSC (11, 12). The NRG1 family of pleiotropic signaling proteins serve as epidermal growth factor (EGF)-like ligands for transmembrane tyrosine kinase receptors of the ErbB family and regulate multiple neurodevelopmental processes, including myelination and synaptic plasticity (13, 14). NRG1 comprises a variety of isoforms, grouped into three main 'types'. NRG1 type I and type II variants contain an immunoglobulin-like domain, whereas type III variants harbor a cysteine-rich domain located N-terminal to the EGF-like domain, which serves as a second transmembrane domain (15). Thus, proteolytic processing in the extracellular domain by several proteases, including β-site amyloid precursor protein–cleaving enzyme1 (BACE1), releases the EGF-like domain in types I and II, resulting in paracrine signaling. In contrast, the EGF-like domain of type III variants remains membrane-anchored following BACE1 cleavage and has been implicated in juxtacrine signaling (16). MNs prominently express NRG1 type III isoforms during perinatal development (17-19). In addition, using an isoform-specific antibody, it has recently been reported that NRG1 type II is targeted to C-boutons (20). Nevertheless, NRG1 isoform-specific functions during C-bouton development have not been addressed.

C-boutons are involved in diseases affecting MNs and spinal cord. Their reversible loss occurs following spinal cord injury (21). Although debated (22), C-boutons have also been reported to display pronounced changes in rodent and human MNs affected by amyotrophic

lateral sclerosis (ALS, (12, 23-27). MN subtype-specific differences in vulnerability during disease conditions are driven by endogenous neuroprotective mechanisms linked to their synaptic activity and excitability, including those related with C-boutons; for example, blocking cholinergic neurotransmission via C-boutons results in increased neurotoxic misfolded SOD1 in MNs of an ALS mouse model (Saxena et al., 2013). Several C-boutons-associated proteins are also directly linked to ALS, as demonstrated for S1R (28-30) and VAPB (31). In addition, a mutation in the ErbB4 receptor has been identified as a genetic cause of ALS (32), suggesting a role of impaired NRG1 signaling in ALS pathophysiology. Another intriguing aspect of C-boutons is the absence of this type of afferent synapses in ALS-resistant MNs of oculomotor (OCM) nuclei (Hellström et al., 2003; Gallart-Palau et al., 2014).

Given the putative relevance of C-boutons for the understanding of spinal cord and MN pathology, and their potential as targets for therapy, a more detailed knowledge of C-bouton organization and reactivity to well-defined conditions of experimental injury is required. For instance, it has not been explored how the arrangement and stability of SSC-associated molecules (i.e., NRG1) are altered when afferent inputs are lost in target-deprived (axotomized) MNs and to which extent the ER-derived C-bouton-associated SSC is altered under these conditions. The effects of axotomy also extend to the perineuronal environment, including synaptic inputs and glial cells. Activated microglia following axotomy appear to displace synaptic terminals from the soma and dendrites, a phenomenon usually recognized as “synaptic striping” (33). C-boutons are also partially lost in response to axotomy (34), and a positive influence of C-bouton sites on recruitment of microglial processes has been observed in axotomized MNs (11). However, the role of microglia in C-bouton disruption and recovery in lesioned MNs is still poorly defined.

Here, we systematically investigated the impact of nerve crush, irreversible peripheral nerve transection and pharmacological induction or attenuation of ER-stress on cholinergic presynaptic terminals, postsynaptic NRG1 clusters, and activation of perisynaptic glial cells. These studies revealed the involvement of ER-stress and microglial activation in pathological C-bouton disruption. In addition, based on findings in transgenic mice overexpressing specific NRG1 isoforms, we show that juxtacrine NRG1 type III accumulates at C-boutons and may act as an organizer of SSC-like ER-plasma membrane contacts. In contrast, paracrine NRG1 type I promotes the differentiation of presynaptic components of C-type synapses, suggesting that distinct NRG1 isoforms govern the architectural and functional organization of C-boutons.

Material and Methods

Animals, surgical procedures and tissue preparation

Wild-type (WT) mice (CD1 strain) were purchased from Harlan Laboratories (Castellar del Vallès, Barcelona, Catalonia, Spain). Mice were housed five to six per cage with permanent access to food and water under a 12-h light/12-h dark. All animal experimentation procedures were performed according to the European Committee Council Directive and the norms established by the *Generalitat de Catalunya* (published as a law in the *Diari Oficial de la Generalitat de Catalunya* [DOGC] 2073, 1995). All experiments were previously evaluated and approved by the Committee for Animal Care and Use of our Universities.

Transgenic mice overexpressing full-length NRG1 type I (35), as well as HA-tagged full-length NRG1 type III (HA-NRG1FL) and a HA-tagged variant that mimics NRG1 type III processing by BACE1 cleavage (HA-NRG1GIEF) were used and genotyped as described previously (36).

All surgical manipulations were performed under anesthesia, with a combination of ketamine (100 mg/Kg) and xylazine (10 mg/Kg). To minimize suffering, mice were subjected to postoperative analgesia with intraperitoneally (i.p.) injected buprenorphine (0.05 mg/Kg). In one group of animals, the sciatic nerve at femoral level was exposed, transected and its proximal stump was ligated in order to prevent spontaneous reinnervation; in another group the sciatic nerve was crushed for 30 seconds using microforceps.

For the pharmacological experiments, mice (postnatal day 60) has been used. Drug delivery regimes were i.p. injected based on published reports (26): methoctramine (Sigma-Aldrich, Madrid, Spain), 200 µg/kg, daily for 15 days; tunicamycin (Sigma-Aldrich), 1 mg/Kg in saline for 2 days; and salubrinal (Alexis Biochemicals, San Diego, CA reconstituted at 2.6mM with PBS containing 0.1%BSA and 10% DMSO) 100 µl, daily , two days before the sciatic nerve axotomy and the next 7 days post-surgery.

Electrical stimulation

We used acupuncture steel needles (0.30x30mm, Acupuncture Shop Aps, Varde, Dennmark) as stimulation electrodes and a Cibertec stimulation unit (CS-20, Cibertec S.A., Madrid, Spain) at both sciatic nerve and spinal cord.

The whole lumbosacral area and the leg were shaved and an incision through the skin and musculature made until visualizing the sciatic nerve. Then electrostimulation (5V at 10 Hz or

100Hz) was applied with the stimulator unit. Electrical stimulation of the sciatic nerve causes action potentials in a retrograde direction which leads to a depolarization of the cell body of the MN in the spinal cord. Direct electrical stimulation of the spinal cord was performed using two acupuncture needles inserted immediately on each side of the dorsal spinal cord. Then, the electrical stimulation was applied with a stimulator unit (5 V at 10 Hz). Three animals in the same conditions but without electrical stimulation were used as sham controls.

In both, sciatic and spinal cord stimulation, an electromyographic record of the food pad was used to check out the electrostimulation accuracy. For this purpose, the recording electrode was inserted into the foot pad and the reference electrode was inserted subcutaneously near the tail.

***In vitro* slices**

The spinal cord, with the pia mater rapidly removed and immersed in cold (0–4 ºC), oxygenated (95% O2/5% CO_2) artificial cerebrospinal fluid (ACSF), containing (in mM): NaCl, 130; $NaHCO_3$, 26; $MgCl_2$, 2; $NaPO_4$, 1.25; $CaCl_2$, 2; KCl, 3; glucose, 10. In some experiments, isolation of spinal cords were performed with sucrose-ACSF (in mM): $NaHCO_3$, 26; $MgCl_2$, 2; $NaPO_4$, 1.25; $CaCl_2$, 0.5; KCl, 3; sucrose, 218, and later transferred to normal ACSF (37). Some experiments were performed in a 0 Ca^{2+} ACSF; in this case, 4 mM EGTA was added. The spinal cord was hydraulically extruded by applying pressure on a syringe filled with ACSF placed on the caudal opening of the vertebral canal as described (38). Prior to excision, the animals were briefly perfused transcardially with ice-cold oxygenated (95% O_2, 5% CO_2) ACSF. Isolated lumbar segments were rapidly sliced (300-400 µm transversal sections) with a McIlwain tissue chopper tissue. The slices were subsequently transferred (or not) to a storage perfusion chamber filled with oxygenated normal ACSF, until their fixation in 4% paraformaldehyde (PF) at the desired experimental time.

Multiple fluorescent labeling and confocal microscopy

Tissue samples were obtained from anaesthetized mice, transcardially perfused with 4% PF in 0.1 M phosphate buffer (PB), pH 7.4. Human spinal cord samples (4% PF fixed) were obtained from the *Banc de Teixits Neurològics de l'Hospital Universitari de Bellvitge* (Dr. Isidre Ferrer, Barcelona, Catalonia, Spain). Tissues from animal species other than rodents were also fixed in 4% PF. Samples were post-fixed overnight in the same fixative at 4°C, and then cryoprotected with 30% sucrose in 0.1 M PB containing 0.02% sodium azide. Transverse cryostat sections (16-µm thick) were collected on gelatin-coated glass slides.

Sections were then permeabilized with phosphate-buffered saline (PBS) containing 0.1% Triton X-100 for 30 minutes, blocked with either 10% normal goat serum or normal horse serum in PBS for 1 h at room temperature, and then incubated overnight at 4 °C with an appropriate primary antibody mixture. The primary antibodies used are indicated in Table 1.

Once previously washed with PBS, sections were incubated for 1 hour with a combination of appropriate secondary fluorescent antibodies labeled with one of the following fluorochromes (1/500): Alexa Fluor 488, Alexa Fluor 546, (Molecular Probes, Eugene, OR, United States), Cy3, or Cy5 (Jackson Immuno Research Laboratories, West Grove, PA, United States). Finally, the spinal cord sections were labeled with blue fluorescent NeuroTrace Nissl staining (1:150; Molecular Probes) and mounted using an anti-fading medium containing 0.1 M Tris-HCl buffer (pH 8.5), 20% glycerol, 10% Mowiol, and 0.1% 1,4-diazabicyclo[2,2,2]octane. For ErbB visualization, some sections were processed using the tyramide signal amplification (TSA), following the procedure recommended by the manufacturer (ThermoFisher, Waltham, MA).

Concerning anti-NRG1 antibodies, in our hands, the best commercially available antibody that can be used to visualize NRG1 at C-boutons is the pan-NRG1 antibody sc-348 (Santa Cruz Biotechnology, Dallas, TX). As this product has been recently discontinued, we looked for other alternatives. Only the rabbit anti-NRG1 type III (extracellular, ANR113, from Alomone, Jerusalem, Israel) gives a positive labeling at C-bouton sites, but this was weaker than that obtained with sc-348. The mouse monoclonal anti-NRG-CDR type III antibody (MABN534, from Millipore, Temecula, CA) is also able to dimly detect C-bouton NRG1 (Suppl. Fig. 1).

Retrograde tracing of MNs was performed with fluorescent-labeled cholera toxin-B subunit (CTB-AlexaFluor 555; Molecular Probes) at 1 µg/µl in PBS. Tracer (5 µl) was injected in leg muscles by means of glass capillary tubes attached to a Hamilton syringe. Animals were perfused 24 h later, and tissues were processed for immunolabeling as above described.

The slides were then examined under a FluoView FV-500 or FluoView FV-1000 Olympus laser-scanning confocal microscopes (Olympus, Hamburg, Germany). The MNs were imaged after obtaining optical sections (0.5 or 1 µm) of cell bodies. Digital images were analyzed with either Visilog 6.3 software (Noesis, Orsay, France) or ImageJ software (US National Institutes of Health, Bethesda, MD, USA). For colocalization analysis, the ImageJ plugin developed by Pierre Bourdoncle (bourdoncle@ijm.jussieu.fr) was used.

Immunolabeled profiles of NRG1 and of the different protein markers examined were then manually counted on the screen for each MN soma. In axotomy experiments, we only analyzed cell bodies located in pes 9 region of L6 spinal cord segment, which corresponds to the sciatic

motor column, according to (39) The area and perimeter of MN somata, and microglial profiles covering MNs were also manually measured. The number of synaptic boutons contacting activated microglia in axotomized MNs was evaluated by image analysis (ImageJ). After application of the outline tool on binarized Iba1 images, these were merged with those corresponding to binarized synaptic boutons: the number of boutons contacting perisomatic microglial profiles was manually counted. In some cases, three-dimensional reconstructions were performed using Bitplane (Imaris, Bitplane, CT, USA) on 0.5-µm thick Z step obtained with the confocal microscope. The digital images were edited using FV10-ASW 3.1 Viewer (Olympus) and Adobe Photoshop CS4 (Adobe Systems Inc, San Jose, CA).

Electron microscopy

Some of the animals were perfused either with 1% PFA and 1% glutaraldehyde in 0.1 M PB (pH 7.4) for conventional electron microscopy or with 4% PFA. Dissected tissues were postfixed in 1% OsO4 and processed for Embed 812 embedding according to standard procedures. Ultrathin sections were counterstained with uranyl acetate and lead citrate.

Statistical analysis

The data are expressed as means ± SEM. The statistical analysis was assessed by either the Student's *t*-test or either one-way or two-way analysis of variance (ANOVA) followed by post-hoc Bonferroni's test. The level of significance was established at $p < 0.05$.

Results

Molecular architecture of C-boutons in vertebrate spinal MNs

In agreement with our previous studies (11), we corroborated that ventral horn α-MNs in adult mouse spinal cord are innervated by large, cholinergic (VAChT-positive) presynaptic terminals, which juxtapose a highly organized postsynaptic compartment harboring a specific set of distinct proteins, including M2 AChRs, Kv2.1 K^+ channels, S1R, and NRG1. Postsynaptic regions delimited by NRG1 were often aligned with several VAChT positive terminal bulbs, indicating that individual C-terminals form branches that share a common postsynapse (Fig. 1a-d). Expression of the NRG1 receptor ErbB2 and its phosphorylated form colocalized with VAChT in the presynaptic compartment of C-boutons (Fig. 1e).

In addition to mouse spinal cord, we observed the characteristic punctate accumulation of NRG1 in the postsynaptic compartment of C-boutons in all vertebrate species analyzed,

including frog, lizard, chicken, pig, and human (Suppl. Fig. 2a-g), consistent with evolutionary conserved NRG1 functions in C-type synapses in the vertebrate lineage.

Upon inspection by electron microscopy (EM), large afferent nerve terminals were identified as C-boutons if they coaligned with a postsynaptic SSC, a hallmark for this type of synapse (Fig. 2a-d). Large aggregates of spherical or flattened clear synaptic vesicles were often concentrated at active zone-like sites close to the presynaptic PM, whereas presumably endocytic "coated" vesicles tended to accumulate at the most peripheral areas of terminals (Fig. 2b). Large membrane-bound vacuoles sequestering synaptic vesicles were also frequently seen within the presynaptic compartment, resembling either late endosomes/multivesicular bodies or phagosomal structures (Fig. 2c). To trace endocytic compartments of MN, intramuscular injections were performed using either fluorescent cholera toxin B or the Hc fragment of tetanus toxin. Although both tracers were extensively incorporated into the vacuolar system of MN somata, no association was found between labeled compartments and NRG1-marked postsynaptic regions of C-boutons (Suppl. Fig. 3).

MN stimulation alters C-bouton-associated NRG1 clusters

We next ask whether physiological or pathological changes in MN activity could affect C-bouton-associated NRG1 expression domains. Electrical stimulation of sciatic nerve results in antidromic propagation of action potentials and MN cell body depolarization, whereas electrical stimulation adjacent to the spinal cord causes orthodromic activation of MN axons that can be assessed by EMG recordings of distal leg and foot muscles. Moderate antidromic stimulation (10 Hz, 60 min) produced a modest increase in the size of both pre- and postsynaptic C-bouton compartments delineated by VAChT and NRG1, respectively (NRG1 cluster size in μm^2: contralateral, 4.26 ± 0.22, n = 28 MNs; ipsilateral, 5.48 ± 0.24, n = 37 MNs; $p < 0.05$). Cholinergic transmission at C-boutons is mediated by M2 AChRs, which can be pharmacologically targeted by treatment with the M2 agonist oxotremorine. Similar to antidromic stimulation, oxotremorine treatment caused an increase in size of postsynaptic NRG1 clusters (NRG1 cluster size in μm^2: saline, 4.37 ± 0.18, n = 103 clusters; oxotremorine, 5.97 ± 0.37, n = 62; $p < 0.01$).

In contrast to moderate stimulation, pathologic antidromic stimulation (100 Hz, 60 min) or direct orthodromic spinal cord stimulation at lower frequency and shorter time period (10 Hz, 30 min) resulted in a severe depletion of NRG1 clusters, whereas VAChT-positive terminals were largely spared (Fig. 3a-k). Examination by EM (Fig. 3j) showed that, as a consequence of extreme spinal cord stimulation, the SSC was disrupted in many C-boutons, and SSC remnants

in identifiable C-boutons had a shortened contact area with the postsynaptic membrane; in line with SSC disruption, we observed an increased number of vacuoles at variable sizes, multivesicular bodies and vesicles in subsynaptic regions of the MN cortical cytoplasm.

ER-disruption was largely confined to cortical regions of MN cell bodies, but was absent from Nissl-like ER stacks located in more central cytoplasmic areas (Fig. 3j). We conclude that pathological exacerbation of synaptic activity at C-boutons heavily impacts on the stability of postsynaptic SSCs. This notion was supported by a dramatic loss of SSC-associated NRG1 clusters at C-boutons in an *in vitro* acute spinal cord slice preparation maintained in ACSF. Even after reducing the preparation time from anesthesia to slicing and paraformaldehyde fixation to ~9 min (with or without ulterior recovery in an oxygenated-superfusion slice chamber), most MNs were completely devoid of NRG1-positive puncta. In those few cases, in which NRG1 clusters persisted, they appeared heavily fragmented and dispersed. Small-sized VAChT puncta were still present juxtaposed to a fraction of de-clustered NRG1-containing SSC remnants (Fig. 3l-s). These findings identify an extreme SSC instability as a major component of adult MN vulnerability in response to slicing procedures, most likely due to their large dendritic arbor (40). While similar experiments performed with Ca^{2+}-free CSF did not improve the preservation of NRG1 clusters (Fig. 3t), we suggest that massive Ca^{2+} release from intracellular Ca^{2+} stores is sufficient to disrupt SSC integrity in cortical areas of MN cell bodies.

To further analyze the dependence of C-boutons and their associated NRG1 clusters on ER integrity *in vivo,* we induced ER-stress by parenteral administration of tunicamycin (26). The effectiveness of drug administration was assessed by the demonstration that BiP was upregulated in MN somata (BiP intensity in arbitrary units: saline, 116.38 ± 6.76, n = 58 MNs; tunicamycin, 217.10 ± 6.42, n = 57 MNs; $p < 0.001$). EM analysis confirmed disrupted Golgi and ER membranes (not shown). Concomitant with widespread ER stress, tunicamycin treatment also disrupted SSC-associated NRG1 clusters (NRG1 cluster size in μm^2: saline, 3.11 ± 0.12, n = 278 clusters [from 58 MNs]; tunicamycin, 2.42 ± 0.06, n = 444 clusters [from 57 MNs], $p < 0.001$), and these postsynaptic changes were matched by an equivalent but attenuated response at the corresponding VAChT-delimited presynaptic terminal (VAChT cluster size in μm^2: saline, 3.73 ± 0.13, n = 514 clusters [from 58 MNs]; tunicamycin, 3.19 ± 0.13, n = 226 clusters [from 57 MNs]; $p < 0.01$). Thus, we conclude that pharmacologically-induced ER-stress diminishes the integrity of SSC-associated NRG1 clusters, which in turn affects the size of presynaptic C-boutons.

Glial reactivity and C-bouton plasticity after reversible and irreversible axonal interruption

Distal axon transection leads to rapid and drastic changes in MNs and their synaptic and glial environment (41). We recently showed that C-boutons of axotomized MNs rapidly attract microglial processes (11). Here, we extended these findings by performing a long-term analysis in both reversible (crush) and irreversible (axotomy) axonal interruption paradigms (Fig. 4a-d). A rapid microglial and astroglial recruitment to MNs occurred 1-3 days after axotomy, in concomitance with C-bouton disruption. Most microglial profiles interacted with NRG1-positive C-boutons 1 day after nerve injury, but subsequently the number of microglia interacting with NRG1-positive C-boutons rapidly declined (Fig. 4e-i, Suppl. Fig. 4 and movie). Importantly, the disruption of VAChT-labeled presynaptic terminals was temporally dissociated from the disorganization of postsynaptic NRG1-clusters. Whereas at 7 days after axotomy we observed a loss of 72% of VAChT profiles, the number of postsynaptic NRG1 clusters was only reduced by 32%. This indicates that the elimination of the presynaptic component of C-boutons implies a disorganization and subsequent reorganization of their postsynaptic SSC-associated NRG1 clusters. A recovery of some C-boutons was seen 15 days after axotomy, which occurred in conjunction with a sustained decline of microglial recruitment. However, an opposite profile was seen for astrogliosis, which, after a transient decline, is again triggered 30 days post irreversible nerve injury (Fig. 4b). Regenerated VAChT-positive C-boutons displayed a marked, but transient, reduction in size of postsynaptic NRG1 clusters (Fig.4b-d). To further assess the involvement of microglia in the elimination of the presynaptic compartment of C-boutons, we compared the juxtaposed expression of VAChT and NRG1 in individual synapses in the presence and absence of nearby Iba1-labeled microglial processes 14 days postaxotomy. NRG1 clusters contacting microglia showed VAChT depletion, whereas those in the absence of microglial processes exhibited a positive VAChT signal (Fig. 4j,k). Together, we conclude that the axotomy-mediated loss of C-boutons is a consequence of a selective microglial recruitment to these synaptic sites, in concordance with the ability of microglia to engulf synaptic inputs during normal and pathological conditions (42, 43).

The pronounced atrophy seen in axotomized non-reinnervating MNs, was less severe after nerve crush (Fig. 4a-d). Moreover, the severe and long-term astroglial reaction following nerve transection was also significantly milder after crush. Compared to irreversible axotomy, an improvement in the restoration of C-bouton density was present 120 days after crush, however, this was no longer sustained.

A further indication of a microglia-mediated removal of presynaptic terminals following axotomy was obtained from ultrastructural analysis (Fig. 5a-k). We noticed that a considerable number of axo-somatic presynaptic terminals showed degenerative changes; some of these

terminals, which often appeared in close proximity to microglial cells, displayed a complete disintegration (Fig 5f and h). However, due to the advanced stage of degeneration, it was impossible to unambiguously identify the morphological subtype of affected synaptic boutons. Nevertheless, in some cases remnants of postsynaptic SSCs were still present adjacent to microglia-covered MN surface areas (or to degenerating synapses), indicating that those correspond to "denervated" C-bouton sites, which underwent degeneration post-axotomy (Fig. 5g and i-k). Based on these data, we conclude that, at least in part, microglia-mediated elimination of C-boutons following axotomy causes a rapid disintegration of presynaptic compartments. This observation contrasts the generally accepted concept that synaptic elimination from axotomized MNs results from the detachment of presynaptic terminals from perykaria by activated microglia, which physically separate pre- and post-synaptic elements in the absence of synaptic degeneration ("synaptic striping", (33)). The exact role of activated microglia in the destruction of synaptic terminals is difficult to assess here. However, PM apposition of microglia to SSC remnants at sites devoid of synaptic boutons most likely marks areas previously occupied by C-boutons, and this finding is consistent with a more rapid postaxotomy loss of VAChT-positive puncta compared to their postsynaptic counterpart as defined by NRG1 immunolabeling.

Neuronal damage induced by peripheral or central axonal injury comprises unfolded protein response and ER-stress that can promote a regenerative response or apoptotic cell death (44, 45). Salubrinal provides neuroprotection by inhibition of P_i-eIF2α dephosphorylation and ER-stress (46) and salubrinal treatment results in attenuation of microgliosis and neurodegeneration in $SOD1^{G93A}$ mice (47). Using a similar treatment protocol we found that salubrinal administration significantly reduced BiP elevation and nearly abolished the massive microglial recruitment to MN somata 7 days post-axotomy (Fig 6a-p). Moreover, the loss of presynaptic VAChT and postsynaptic NRG1 that concomitantly occurred in axotomyzed MNs was strongly attenuated by salubrinal. This indicates that unfolded protein response is coupled with microglial activation and synaptic loss in distally lesioned MNs.

Distinct NRG1 isoforms mediate specific pre- and postsynaptic functions at cholinergic C-boutons

Transgenic mice with Thy1.2 promoter-mediated neuronal overexpression of distinct NRG1 isoforms have previously been employed to study axonal control mechanisms during myelination of spinal MNs (35, 36). Considering NRG1 as a prominent and spatially restricted component of C-boutons, we took advantage of these mouse lines to examine NRG1 isoform-

specific functions in C-bouton development and architecture. These studies included transgenic mice which overexpress full-length NRG1 type I (35), N-terminally HA epitope-tagged full-length NRG1 type III (HA-NRG1^{FL}) or a HA-tagged NRG1 type III variant that mimics the product of BACE1 cleavage in the juxtamembrane 'stalk' region (HA-NRG1^{GIEF}; (36), which separates an N-terminal (EGF-like domain-containing) transmembrane protein from the C-terminal ICD (Suppl. Fig. 5).

First, we performed simultaneous fluorescent immunostainings for the N-terminal HA-tag and either the C-terminal ICD of NRG1 or the C-bouton postsynaptic markers S1R, Kv2.1 and M2 AChR, in conjunction with presynaptic VAChT on spinal cord sections (Fig. 7a-f). Samples from HA-NRG1^{FL} mice showed highly overlapping immunostaining for the HA-tag and the ICD on the surface of MN cell bodies, which was frequently associated with presynaptic VAChT-positive C-boutons (Fig. 7a). These findings are consistent with the accumulation of unprocessed NRG1 type III at postsynaptic sites of C-boutons. To assess possible consequences of the postsynaptic accumulation of NRG1 type III on the organization of C-type synapses, we performed an examination of HA-NRG1^{FL} mice by EM. Remarkably, we observed an accumulation of abnormally expanded surface-associated ER membranes, which were arranged like redundant SSCs (Fig. 9a). As the number of cholinergic C-boutons contacting MN somata was not altered (Fig. 8a), only a fraction of plasma membrane presenting apposed ER membranes was associated with afferent synaptic C-boutons in HA-NRG1^{FL} mice. We also analyzed whether the pattern of S1R and Kv2.1, two molecules that normally concentrate in C-bouton-associated SSCs, were altered in HA-NRG1^{FL} mice. We found that both, S1R and Kv2.1, were notably increased, displaying a similar pattern to that found for NRG1 type III detected by HA staining (Fig. 7b and e, and 8d and e). Thus, the induction of redundant SSC-like membrane compartments by NRG1 type III overexpression was linked to an increased production and insertion of other SSC-associated partner molecules, such as S1R and Kv2.1. Nevertheless, a more detailed examination revealed that although S1R and NRG1 were closely associated, they did not occupy identical micro-domains (Fig. 8c-d), very similar to their configuration in C-boutons from WT mice (11). In contrast, a tight co-localization between NRG1 and Kv2.1 was observed (Fig. 7e). Importantly, expression of M2 muscarinic receptors, which presumably reside mainly in the postsynaptic membrane, also expanded beyond synaptic areas, as defined by the absence of VAChT-positive terminals, in HA-NRG1^{FL} mice (Fig. 7f and 8c). Together, the redundancy and enlargement of SSC-like structures in HA-NRG1^{FL} mice suggest that full-length NRG1 type III acts as an organizer of ER-membrane contacts, including SSCs, in α–MNs. These findings also indicate that SSCs are involved in organizing the size and molecular layout of the

postsynaptic membrane, whereas SSC architecture has no major direct effects on presynaptic elements of C-boutons.

To address a specific role of the cytoplasmic ICD in organizing SSC architecture in C-boutons, we next investigated HA-NRG1^{GIEF} mice. Although extensive HA-NRG1^{GIEF} expression was observed in MN cell bodies and dendrites, the BACE1-processed variant of NRG1 type III was completely excluded from C-bouton sites. This was unambiguously corroborated when HA-tag detection was combined with antibodies against VAChT and pan-NRG1 (sc-348) to localize C-boutons (Fig. 7g). Consistent with this finding, no expansion of SCC structures, S1R and M2 expression domains was observed in HA-NRG1^{GIEF} mice (not shown). Taken together, these data strongly suggest that the C-terminal ICD is required for SSC accumulation of NRG1 type III and that full-length NRG1 type III exerts specific postsynaptic, SSC organizing functions in spinal α–MNs.

NRG1 type I shares the same ICD with NRG1 type III, but lacks a second transmembrane domain, therefore BACE1 processing results in shedding of the N-terminal EGF-like domain and paracrine signaling. To identify possible consequences of enhanced NRG1 type I-mediated paracrine signaling on C-bouton development, we next examined transgenic mice with Thy1.2 promoter-driven NRG1 type I overexpression (*NRG1^{typeI}*) in spinal MNs (35). As this transgene lacks an N-terminal HA-tag, a specific immunostaining for transgene-derived NRG1 type I could not be performed. However, immunostaining for the ICD produced an extensive signal at the MN surface of *NRG1^{typeI}* mice (Fig. 7h) analogous to that obtained in *HA-NRG1^{FL}* mice. Moreover, immunostaining for M2 AChRs showed their enlarged distribution on the MN surface, similar to that observed in *HA-NRG1^{FL}* mice (Fig. 7i). However, in stark contrast to *HA-NRG1^{FL}* mice, VAChT immunostaining revealed a profound increase in the number and size of presynaptic cholinergic terminals innervating the MN surface (Fig. 8a, b). Nevertheless, we found no concomitant increase in the number of ChAT-positive V0$_C$ neurons in *NRG1^{typeI}* mice (V0$_C$ interneuron numbers per section, expressed as mean ± SEM: WT, 2.37 ± 0.32, n = 8 sections; *NRG1^{typeI}* 1.74 ± 0.32, n = 14 sections; $p > 0.05$), strongly suggesting that C-bouton synaptogenesis was abnormally stimulated in *NRG1^{typeI}* mice. Many of these VAChT-positive puncta were associated with neighboring postsynaptic S1R-positive patches, which did not overlap with pan-NRG1 signal, in the same way as occurs in WT (Fig. 7h). In addition, S1R clusters in *NRG1^{typeI}* mice were not enlarged when compared with those in WT (Fig. 8d). This is in contrast to that was observed in *HA-NRG1^{FL}* mice, in which surface-associate S1R labeling is largely expanded together with NRG1. Kv2.1 clusters were not detected in *NRG1^{typeI}* mouse MNs (Fig. 8e).

Ultrastructural examination confirmed the presence of enlarged presynaptic terminals on the MN soma surface, matching only partially with post-synaptic SSC; moreover, the amplified formation of SSC-like ER-plasma membrane contacts in *HA-NRG1*^{FL} mice was not observed in *NRG1*^{typeI} mice (Fig. 9b). This suggests that NRG1 type I is mainly targeted to the MN plasma membrane, whereas NRG1 type III is preferentially located to C-bouton SSCs. As Kv2.1 is a protein specifically linked to ER-plasma-membrane junctions (e.g. at SSCs) (48), its expanded or, alternatively, reduced expression detected in *HA-NRG1*^{FL} or *NRG1*^{typeI} mice, respectively, is consistent with this interpretation. A summary of idealized C-bouton phenotypes in NRG1 transgenic mice is depicted in Fig. 9c.

C-boutons and associated NRG1 clusters are absent in ALS-resistant OCM (abducens cranial nerve [CN] VI) MNs (12), but present in other brainstem motor nuclei. Therefore, we next examined the impact of NRG1 overexpression in brainstem MNs of NRG1 transgenic mouse lines (Suppl. Fig. 6a-f). Consistent with our above findings, non-OCM MNs (facial [CNVII], hypoglossus [CNXII] and ambiguous [CNX] nuclei) displayed similar effects of NRG1 overexpression on C-bouton structure as described for spinal cord MNs, including an increased number of VAChT-containing synaptic afferents in NRG1 type I overexpressing transgenic mice (Suppl. Fig. 6c). NRG1 labeling patterns in OCM MNs of *NRG1*^{typeI} *HA-NRG1*^{FL} mice were also comparable to those observed in non-OCM MNs. However, as in WT (Suppl. Fig. 6d), we never observed VAChT-positive C-boutons on the surface of transgenic OCM MNs (Suppl. Fig. 6e-f). These findings strongly suggest that NRG1 type I promotes C-bouton synaptogenesis also at non-OCM MNs, but that additional factors are required to promote cholinergic synaptogenesis in OCM MNs.

Altogether, these findings suggest that: 1) full-length NRG1 type III acts as a specific organizer of postsynaptic SSC-like membrane compartments without a major impact on the C-bouton presynaptic counterpart, 2) NRG1 type I promotes presynaptic C-bouton synaptogenesis, with no influence on biogenesis or molecular architecture of co-aligned SSC, and 3) there is partial independence of pre- and postsynaptic C-bouton development. Thus, specific signaling functions related to the distinct spatial arrangement of NRG1 isoforms are involved in the complex matching of pre- and postsynaptic elements at C-boutons.

Discussion

To provide a better understanding of the role of C-boutons and associated NRG1 assemblies in MN diseases, we describe here novel aspects of their biology and responses when subjected to

distinct paradigms of experimental MN injury. Stimulation and *ex vivo* slicing experiments revealed that C-bouton-associated NRG1 assemblies are extremely sensitive to acute cellular stress. This probably reflects their tight association with SSCs, a specialized form of highly dynamic cortical ER, which is closely apposed to the postsynaptic plasma membrane of C-boutons. In fact, rapid and reversible ER fission occurs after neuronal depolarization, and synaptic activity modulates ER structure via Ca^{2+} transients (49, 50). In addition, Kv2.1 clusters in ER-plasma-membrane junctions, which are homologous structures to SSCs, are highly dynamic and unstable when exposed to moderate stress (48). We report here that moderate levels of either electrical or chemical stimulation induce an enlargement of VAChT-labeled presynaptic terminals and their associated postsynaptic NRG1 clusters. This is in congruence with data reported in the context of electrical stimulation of proprioceptive afferents to MNs (51). The dependence of NRG1 clusters on the structural integrity of cortical ER was further confirmed by induction of ER-stress with tunicamycin, which severely disrupted NRG1 clusters without affecting the number and size of VAChT-positive terminals. This observation is distinct from our findings in MNs following axotomy in which the dispersion of NRG1 clusters at C-boutons takes place at a slower time scale compared to the loss of presynaptic terminals, the latter presumably being mediated by reactive microglia.

We also confirm our previous observations that C-boutons are preferred sites to be contacted by reactive microglia in injured MNs post-axotomy (11) and provide new data concerning the involvement of microglial cells in synaptic removal in this pathological condition. At present, the molecular substrate of this positive chemotactic effect is unknown. NRG1/ErbB signaling promotes microglial chemotaxis *in vitro* and in spinal cord dorsal horn after peripheral nerve injury (52, 53), and antagonizing NRG1 signaling results in a reduction of microgliosis and MN death in mutant SOD1 ALS mice (54). Thus, whether NRG1/ErbB signaling also operates during C-bouton-directed microglial sensing after axotomy should be further explored.

We found no evidence for the engulfment of presynaptic elements by microglial processes recruited in the vicinity of axotomyzed MNs. This is in accordance with the classical description of microglial activation and synaptic removal that occurs during the response of MN cell bodies to axotomy (33). However, in contrast to these studies, we unambiguously observed degenerating presynaptic boutons contacting lesioned MNs in close association with perineuronally-recruited microglia. This suggests an active role of microglia in the disintegration of presynaptic terminals by means of a target-directed toxic mechanism instead of bulk phagocytosis. Activated microglia produce free oxygen radicals, nitric oxide, proteases

and cytokines (55), all of which could be neurotoxic in a local microenvironment and induce extrinsic apoptosis (56) or extracellular digestion ("exophagy") of synaptic debris (57). In congruence with this idea, superoxide ions produced by microglial cells induce apoptotic death of Purkinje neurons in organotypic slice cultures (58), and macrophage-derived TNFα signals developmental MN death (59). Since axons can activate degenerative/apoptotic molecular pathways without resulting in cell death of the parent neuron (60), it is plausible that a similar, spatially restricted mechanism operates at presynaptic axon terminals (61).

Our data suggest that NRG1 'declustering' is related to a microglia-dependent disruption of cholinergic presynaptic terminals, in conjunction with ER-stress/reorganization inherent to a chromatolytic reaction. We demonstrate that C-bouton disruption in axotomyzed MNs is prevented when ER-stress or microglial activation is inhibited by salubrinal treatment. Our data also indicate that removal of afferent terminals, including C-boutons, precedes postsynaptic NRG1 declustering and removal. This interpretation is supported by the presence of activated microglia in close proximity to denervated, SSC-containing postsynaptic sites of MN somata. Resting microglia perform specific and transient mutual contacts and serve as a vigilant surveyor of synaptic activity. During pathological conditions, microglial processes extensively enwrap synaptic boutons that will be later removed (42). However, in agreement with a classic study (33), we found no ultrastructural evidence for the engulfment of embraced axon terminals into phagosomes of activated microglia adjacent to axotomyzed MN somata.

Axonal regeneration following nerve crush frequently results in restored peripheral nerve function 6-8 weeks after injury (34, 62). Our analysis of cholinergic C-boutons are comparable with previous studies (34) showing their recovery after either irreversible transection or crush. However, to which extend their function is restored is currently unclear. In fact, the size of postsynaptic NRG1 clusters was not fully restored after irreversible nerve transection, but almost completely reestablished after (more permissive) injury following nerve crush. This is another example of the relative independence of pre- and postsynaptic components of C-boutons during development and adult plasticity. C-bouton density in MNs also depends on competition with other types of synapses in an activity and space-dependent manner (63). For instance, the loss of vesicular glutamate transporter 1 (VGLUT1)-containing boutons (derived from proprioceptive sensory afferents) from axotomyzed MNs is not restored during peripheral regeneration (34). This indicates that peripheral nerve injury induces permanent deficits in the function and plasticity of central synaptic connections, but the inability to restore proprioceptive afferent may favor regeneration of cholinergic inputs to lesioned MNs.

Our findings in NRG1 transgenic mice demonstrate that altered expression levels (and most likely signaling activities) of NRG1 isoforms differentially affect molecular and structural features of C-boutons. These results reveal a previously unknown role of distinct NRG1 isoforms as selective organizers of pre- and post-synaptic components of cholinergic C-boutons at the receptive somatodendritic compartment of spinal MNs and adds to established functions of NRG1 in the neuromuscular system, such as: 1) differentiation and survival of Schwann cells (64); 2) myelination of peripheral axons (35, 36, 65, 66); 3) terminal Schwann cell-mediated remodeling of neuromuscular junctions (19); and 4) regulation nicotinic AChRs clustering at the neuromuscular junction (67).

Specifically, we show that NRG1 type III serves as a postsynaptic SSC organizer with no major impact on the formation or structure of presynaptic VAChT-positive terminals. In contrast, NRG1 type I stimulates a substantial increase in the number and size of cholinergic inputs without driving the development of an equally enlarged SSC. The exact mechanism and functional consequences of NRG1 type I-mediated effects on presynaptic terminal growth and NRG1 type III-induced SSC enlargement are currently unknown and require further investigation. ER-plasma membrane contacts are involved in calcium homeostasis by means of a mechanism referred to as “store operated calcium entry” (SOCE). An essential protein in this process is STIM1, which, when overexpressed, induces multilayered stacks of cortical ER (68) comparable to those produced in MNs of NRG1 type III overexpressing mice. In our study, enlarged ER-derived planar stacks displayed distinct subdomains that, in addition to NRG1, were enriched in SR1 and Kv2.1, as expected for redundant SSCs. It is interesting to note that the sole overexpression of Kv2.1 is sufficient to induce ER-plasma-membrane junctions (48). Since S1R plays a role as a SOCE regulator in a variety of systems, this suggests that SSC at C-boutons serve as a Ca^{2+} microdomain and that NRG1 type III-mediated changes of SSC architecture could recruit STIM1 functions, thereby shaping the temporal and spatial fine-tuning of intracellular Ca^{2+} at this specific site (69). Stimulation of both NRG1 type I and type III-mediated signaling impacts on the accumulation of M2 AChRs at the postsynaptic plasma membrane. Thus, the concept of NRG1-regulated functional interactions of M2 AChRs with other postsynaptic components of C-type synapses, e. g. Kv2.1 potassium channels (7) requires further investigations. Kv2.1 channels form highly dynamic clusters on the plasma membrane of cortical neurons (70), may contribute to homeostatic adaptation of MN excitability during pathologic conditions, and axotomy results in a loss of Kv2.1 clusters at C-boutons (71). Of note, NRG2, which is structurally related to NRG1 type I, accumulates in close proximity to Kv2.1 clusters in the plasma membrane atop intracellular SSCs in cortical interneurons and

NRG2/ErbB4 serve a negative feedback loop that controls NMDA function (72). Moreover, NRG1 type I colocalizes with NRG2 and Kv2.1 channel clusters in cultured hippocampal neurons (20). These findings indicate that NRG isoforms constitute a diverse set of spatially compartmentalized postsynaptic signaling molecules that play an important role during C-bouton differentiation. Possible additional functions in the modulation of plasma membrane/SSC interactions and chemical transmission at C-boutons and cortical synapses will require further studies.

Altered spinal cord expression of NRG1 isoforms occurs in a SOD1 ALS mouse model (73), and loss of C-bouton-associated NRG1 assemblies in this mouse model and in human ALS have been observed (12, 74). Similarly, increased activation of ErbB receptors was found in inflammatory microglia in ALS mouse models and human patients (73, 75). Recently, NRG1 signaling was directly targeted in SOD1-ALS mice by virus-mediated delivery of NRG1 type III to the spinal cord, which resulted in an extended survival time and reduced C-bouton loss, whereas NRG1 type I expression had no effect (74). NRG1 type I overexpression confined to the muscle promoted axonal collateral sprouting and muscle reinnervation, but failed to improve clinical outcome (76). On the other hand, blocking NRG1 signaling reduced microglial activation and slowed disease progression (54). Taken together, these data indicate that pleiotropic NRG1 activities may account for the variable and to some extend discrepant outcomes when analyzed in the context of distinct therapeutic approaches.

In conclusion, our study identifies plastic C-bouton changes in well-defined experimental models of MN injury and reveals previously unknown functions of distinct NRG1 isoforms in C-bouton architecture. Our data provide a refined framework for the involvement of C-boutons in the pathophysiology of MN diseases, such as ALS. Since C-boutons regulate MN excitability, contribute to MN vulnerability and orchestrate neuroinflammatory glial responses after nerve injury, the targeting of C-bouton-embedded signaling modules, such as the NRG1/ErbB axis, should be further explored in support of novel treatment strategies for ALS and other MN disorders.

Acknowledgements

We would like to thank Klaus A. Nave for advice and kindly supplying NRG1 mutant mice, Jesús María López, Ester Desfilis and José Antonio Moreno for providing spinal cord samples from non-rodent animals. Anaïs Panosa and Xavier Calomarde for technical support with confocal and electron microscopy, and the SCT animal facility of the University of Lleida for

mouse care and housing. This work was supported by grants to JEE and JC from the Spanish *Ministerio de Economía y Competitividad* co-financed by FEDER (SAF2015-70801-R). SS holds a grant from Spanish *Ministerio de Educación, Cultura y Deporte* (FPU). MHS holds a Heisenberg Fellowship from the Deutsche Forschungsgemeinschaft (DFG) and acknowledges funding by a DFG research grant (SCHW741/4-1).

Author contributions: JEE, MHS, AC and JC conceived and designed research. SS, AC, OT, LP, MCS-B, MS, SH and JEE performed research. AC, SS, JC, MHS and JEE analyzed data. JEE, JC, AC and MHS wrote the paper.

Conflict of interest: The authors declare that no conflict of interest exists.

References

1. Rekling, J. C., Funk, G. D., Bayliss, D. A., Dong, X. W., and Feldman, J. L. (2000) Synaptic control of motoneuronal excitability. *Physiol Rev* **80**, 767-852
2. Kanning, K. C., Kaplan, A., and Henderson, C. E. (2010) Motor neuron diversity in development and disease. *Annu Rev Neurosci* **33**, 409-440
3. Miles, G. B., Hartley, R., Todd, A. J., and Brownstone, R. M. (2007) Spinal cholinergic interneurons regulate the excitability of motoneurons during locomotion. *Proc Natl Acad Sci U S A* **104**, 2448-2453
4. Zagoraiou, L., Akay, T., Martin, J. F., Brownstone, R. M., Jessell, T. M., and Miles, G. B. (2009) A cluster of cholinergic premotor interneurons modulates mouse locomotor activity. *Neuron* **64**, 645-662
5. Conradi, S. (1969) Ultrastructure of dorsal root boutons on lumbosacral motoneurons of the adult cat, as revealed by dorsal root section. *Acta Physiol Scand Suppl* **332**, 85-115
6. Hellström, J., Oliveira, A. L. R., Meister, B., and Cullheim, S. (2003) Large cholinergic nerve terminals on subsets of motoneurons and their relation to muscarinic receptor type 2. *Journal of Comparative Neurology* **460**, 476-486
7. Muennich, E. A., and Fyffe, R. E. (2004) Focal aggregation of voltage-gated, Kv2.1 subunit-containing, potassium channels at synaptic sites in rat spinal motoneurones. *J Physiol* **554**, 673-685

8. Deardorff, A. S., Romer, S. H., Deng, Z., Bullinger, K. L., Nardelli, P., Cope, T. C., and Fyffe, R. E. (2013) Expression of postsynaptic Ca2+-activated K+ (SK) channels at C-bouton synapses in mammalian lumbar α-motoneurons. *J Physiol* **591**, 875-897
9. Mavlyutov, T. A., Epstein, M. L., Verbny, Y. I., Huerta, M. S., Zaitoun, I., Ziskind-Conhaim, L., and Ruoho, A. E. (2013) Lack of sigma-1 receptor exacerbates ALS progression in mice. *Neuroscience* **240**, 129-134
10. Deardorff, A. S., Romer, S. H., Sonner, P. M., and Fyffe, R. E. (2014) Swimming against the tide: investigations of the C-bouton synapse. *Front Neural Circuits* **8**, 106
11. Casanovas, A., Salvany, S., Lahoz, V., Tarabal, O., Piedrafita, L., Sabater, R., Hernandez, S., Caldero, J., and Esquerda, J. E. (2017) Neuregulin 1-ErbB module in C-bouton synapses on somatic motor neurons: molecular compartmentation and response to peripheral nerve injury. *Sci Rep* **7**, 40155
12. Gallart-Palau, X., Tarabal, O., Casanovas, A., Sabado, J., Correa, F. J., Hereu, M., Piedrafita, L., Calderó, J., and Esquerda, J. E. (2014) Neuregulin-1 is concentrated in the postsynaptic subsurface cistern of C-bouton inputs to alpha-motoneurons and altered during motoneuron diseases. *Faseb Journal* **28**, 3618-3632
13. Buonanno, A., and Fischbach, G. D. (2001) Neuregulin and ErbB receptor signaling pathways in the nervous system. *Curr Opin Neurobiol* **11**, 287-296
14. Mei, L., and Nave, K. A. (2014) Neuregulin-ERBB signaling in the nervous system and neuropsychiatric diseases. *Neuron* **83**, 27-49
15. Wolpowitz, D., Mason, T. B., Dietrich, P., Mendelsohn, M., Talmage, D. A., and Role, L. W. (2000) Cysteine-rich domain isoforms of the neuregulin-1 gene are required for maintenance of peripheral synapses. *Neuron* **25**, 79-91
16. Willem, M. (2016) Proteolytic processing of Neuregulin-1. *Brain Res Bull* **126**, 178-182
17. Meyer, D., Yamaai, T., Garratt, A., Riethmacher-Sonnenberg, E., Kane, D., Theill, L. E., and Birchmeier, C. (1997) Isoform-specific expression and function of neuregulin. *Development* **124**, 3575-3586
18. Yang, X., Kuo, Y., Devay, P., Yu, C., and Role, L. (1998) A cysteine-rich isoform of neuregulin controls the level of expression of neuronal nicotinic receptor channels during synaptogenesis. *Neuron* **20**, 255-270
19. Lee, Y. I., Li, Y., Mikesh, M., Smith, I., Nave, K. A., Schwab, M. H., and Thompson, W. J. (2016) Neuregulin1 displayed on motor axons regulates terminal Schwann cell-mediated synapse elimination at developing neuromuscular junctions. *Proceedings of the National Academy of Sciences of the United States of America* **113**, E479-E487

20. Vullhorst, D., Ahmad, T., Karavanova, I., Keating, C., and Buonanno, A. (2017) Structural Similarities between Neuregulin 1-3 Isoforms Determine Their Subcellular Distribution and Signaling Mode in Central Neurons. *Journal of Neuroscience* **37**, 5232-5249
21. Kitzman, P. (2006) Changes in vesicular glutamate transporter 2, vesicular GABA transporter and vesicular acetylcholine transporter labeling of sacrocaudal motoneurons in the spastic rat. *Exp Neurol* **197**, 407-419
22. Dukkipati, S. S., Chihi, A., Wang, Y., and Elbasiouny, S. M. (2017) Experimental Design and Data Analysis Issues Contribute to Inconsistent Results of C-Bouton Changes in Amyotrophic Lateral Sclerosis. *eNeuro* **4**
23. Nagao, M., Misawa, H., Kato, S., and Hirai, S. (1998) Loss of cholinergic synapses on the spinal motor neurons of amyotrophic lateral sclerosis. *J Neuropathol Exp Neurol* **57**, 329-333
24. Pullen, A. H., and Athanasiou, D. (2009) Increase in presynaptic territory of C-terminals on lumbar motoneurons of G93A SOD1 mice during disease progression. *Eur J Neurosci* **29**, 551-561
25. Herron, L. R., and Miles, G. B. (2012) Gender-specific perturbations in modulatory inputs to motoneurons in a mouse model of amyotrophic lateral sclerosis. *Neuroscience* **226**, 313-323
26. Saxena, S., Roselli, F., Singh, K., Leptien, K., Julien, J. P., Gros-Louis, F., and Caroni, P. (2013) Neuroprotection through Excitability and mTOR Required in ALS Motoneurons to Delay Disease and Extend Survival. *Neuron* **80**, 80-96
27. Milan, L., Courtand, G., Cardoit, L., Masmejean, F., Barriere, G., Cazalets, J. R., Garret, M., and Bertrand, S. S. (2015) Age-Related Changes in Pre- and Postsynaptic Partners of the Cholinergic C-Boutons in Wild-Type and SOD1G93A Lumbar Motoneurons. *PLoS One* **10**, e0135525
28. Luty, A. A., Kwok, J. B., Dobson-Stone, C., Loy, C. T., Coupland, K. G., Karlstrom, H., Sobow, T., Tchorzewska, J., Maruszak, A., Barcikowska, M., Panegyres, P. K., Zekanowski, C., Brooks, W. S., Williams, K. L., Blair, I. P., Mather, K. A., Sachdev, P. S., Halliday, G. M., and Schofield, P. R. (2010) Sigma nonopioid intracellular receptor 1 mutations cause frontotemporal lobar degeneration-motor neuron disease. *Ann Neurol* **68**, 639-649
29. Al-Saif, A., Al-Mohanna, F., and Bohlega, S. (2011) A mutation in sigma-1 receptor causes juvenile amyotrophic lateral sclerosis. *Ann Neurol* **70**, 913-919

30. Mavlyutov, T. A., Guo, L. W., Epstein, M. L., and Ruoho, A. E. (2015) Role of the Sigma-1 receptor in Amyotrophic Lateral Sclerosis (ALS). *J Pharmacol Sci* **127**, 10-16
31. Aliaga, L., Lai, C., Yu, J., Chub, N., Shim, H., Sun, L., Xie, C., Yang, W. J., Lin, X., O'Donovan, M. J., and Cai, H. (2013) Amyotrophic lateral sclerosis-related VAPB P56S mutation differentially affects the function and survival of corticospinal and spinal motor neurons. *Hum Mol Genet* **22**, 4293-4305
32. Takahashi, Y., Fukuda, Y., Yoshimura, J., Toyoda, A., Kurppa, K., Moritoyo, H., Belzil, V. V., Dion, P. A., Higasa, K., Doi, K., Ishiura, H., Mitsui, J., Date, H., Ahsan, B., Matsukawa, T., Ichikawa, Y., Moritoyo, T., Ikoma, M., Hashimoto, T., Kimura, F., Murayama, S., Onodera, O., Nishizawa, M., Yoshida, M., Atsuta, N., Sobue, G., Fifita, J. A., Williams, K. L., Blair, I. P., Nicholson, G. A., Gonzalez-Perez, P., Brown, R. H., Nomoto, M., Elenius, K., Rouleau, G. A., Fujiyama, A., Morishita, S., Goto, J., Tsuji, S., and JaCALS. (2013) ERBB4 Mutations that Disrupt the Neuregulin-ErbB4 Pathway Cause Amyotrophic Lateral Sclerosis Type 19. *American Journal of Human Genetics* **93**, 900-905
33. Blinzinger, K., and Kreutzberg, G. (1968) Displacement of synaptic terminals from regenerating motoneurons by microglial cells. *Z Zellforsch Mikrosk Anat* **85**, 145-157
34. Alvarez, F. J., Titus-Mitchell, H. E., Bullinger, K. L., Kraszpulski, M., Nardelli, P., and Cope, T. C. (2011) Permanent central synaptic disconnection of proprioceptors after nerve injury and regeneration. I. Loss of VGLUT1/IA synapses on motoneurons. *J Neurophysiol* **106**, 2450-2470
35. Michailov, G. V., Sereda, M. W., Brinkmann, B. G., Fischer, T. M., Haug, B., Birchmeier, C., Role, L., Lai, C., Schwab, M. H., and Nave, K. A. (2004) Axonal neuregulin-1 regulates myelin sheath thickness. *Science* **304**, 700-703
36. Velanac, V., Unterbarnscheidt, T., Hinrichs, W., Gummert, M. N., Fischer, T. M., Rossner, M. J., Trimarco, A., Brivio, V., Taveggia, C., Willem, M., Haass, C., Mobius, W., Nave, K. A., and Schwab, M. H. (2012) Bace1 processing of NRG1 type III produces a myelin-inducing signal but is not essential for the stimulation of myelination. *Glia* **60**, 203-217
37. Carp, J. S., Tennissen, A. M., Mongeluzi, D. L., Dudek, C. J., Chen, X. Y., and Wolpaw, J. R. (2008) An in vitro protocol for recording from spinal motoneurons of adult rats. *J Neurophysiol* **100**, 474-481
38. Chery, N., Yu, X. H., and de Koninck, Y. (2000) Visualization of lamina I of the dorsal horn in live adult rat spinal cord slices. *J Neurosci Methods* **96**, 133-142
39. Watson, C., Paxinos, G., G., K., and Heise, C. (2009) *The spinal cord*, Elsevier, Amsterdam

40. Moghaddasi, M., Velumian, A. A., Zhang, L., and Fehlings, M. G. (2007) An ex vivo preparation of mature mice spinal cord to study synaptic transmission on motoneurons. *J Neurosci Methods* **159**, 1-7
41. Aldskogius, H., and Kozlova, E. N. (1998) Central neuron-glial and glial-glial interactions following axon injury. *Progress in neurobiology* **55**, 1-26
42. Wake, H., Moorhouse, A. J., Jinno, S., Kohsaka, S., and Nabekura, J. (2009) Resting microglia directly monitor the functional state of synapses in vivo and determine the fate of ischemic terminals. *The Journal of neuroscience : the official journal of the Society for Neuroscience* **29**, 3974-3980
43. Schafer, D. P., Lehrman, E. K., Kautzman, A. G., Koyama, R., Mardinly, A. R., Yamasaki, R., Ransohoff, R. M., Greenberg, M. E., Barres, B. A., and Stevens, B. (2012) Microglia sculpt postnatal neural circuits in an activity and complement-dependent manner. *Neuron* **74**, 691-705
44. Penas, C., Pascual-Font, A., Mancuso, R., Fores, J., Casas, C., and Navarro, X. (2011) Sigma receptor agonist 2-(4-morpholinethyl)1 phenylcyclohexanecarboxylate (Pre084) increases GDNF and BiP expression and promotes neuroprotection after root avulsion injury. *Journal of neurotrauma* **28**, 831-840
45. Li, S., Yang, L., Selzer, M. E., and Hu, Y. (2013) Neuronal endoplasmic reticulum stress in axon injury and neurodegeneration. *Annals of neurology* **74**, 768-777
46. Boyce, M., Bryant, K. F., Jousse, C., Long, K., Harding, H. P., Scheuner, D., Kaufman, R. J., Ma, D., Coen, D. M., Ron, D., and Yuan, J. (2005) A selective inhibitor of eIF2alpha dephosphorylation protects cells from ER stress. *Science* **307**, 935-939
47. Saxena, S., Cabuy, E., and Caroni, P. (2009) A role for motoneuron subtype-selective ER stress in disease manifestations of FALS mice. *Nature neuroscience* **12**, 627-636
48. Fox, P. D., Haberkorn, C. J., Akin, E. J., Seel, P. J., Krapf, D., and Tamkun, M. M. (2015) Induction of stable ER-plasma-membrane junctions by Kv2.1 potassium channels. *Journal of cell science* **128**, 2096-2105
49. Kucharz, K., Krogh, M., Ng, A. N., and Toresson, H. (2009) NMDA receptor stimulation induces reversible fission of the neuronal endoplasmic reticulum. *PLoS One* **4**, e5250
50. Kucharz, K., Wieloch, T., and Toresson, H. (2011) Potassium-induced structural changes of the endoplasmic reticulum in pyramidal neurons in murine organotypic hippocampal slices. *J Neurosci Res* **89**, 1150-1159
51. Gajewska-Wozniak, O., Grycz, K., Czarkowska-Bauch, J., and Skup, M. (2016) Electrical Stimulation of Low-Threshold Proprioceptive Fibers in the Adult Rat Increases Density

of Glutamatergic and Cholinergic Terminals on Ankle Extensor alpha-Motoneurons. *PLoS One* **11**, e0161614

52. Calvo, M., Zhu, N., Tsantoulas, C., Ma, Z., Grist, J., Loeb, J. A., and Bennett, D. L. (2010) Neuregulin-ErbB signaling promotes microglial proliferation and chemotaxis contributing to microgliosis and pain after peripheral nerve injury. *The Journal of neuroscience : the official journal of the Society for Neuroscience* **30**, 5437-5450
53. Calvo, M., Zhu, N., Grist, J., Ma, Z., Loeb, J. A., and Bennett, D. L. (2011) Following nerve injury neuregulin-1 drives microglial proliferation and neuropathic pain via the MEK/ERK pathway. *Glia* **59**, 554-568
54. Liu, M., Solomon, W., Cespedes, J. C., Wilson, N. O., Ford, B., and Stiles, J. K. (2018) Neuregulin-1 attenuates experimental cerebral malaria (ECM) pathogenesis by regulating ErbB4/AKT/STAT3 signaling. *J Neuroinflammation* **15**, 104
55. Madry, C., Kyrargyri, V., Arancibia-Carcamo, I. L., Jolivet, R., Kohsaka, S., Bryan, R. M., and Attwell, D. (2018) Microglial Ramification, Surveillance, and Interleukin-1beta Release Are Regulated by the Two-Pore Domain K(+) Channel THIK-1. *Neuron* **97**, 299-312 e296
56. Galluzzi, L., Vitale, I., Aaronson, S. A., Abrams, J. M., Adam, D., Agostinis, P., Alnemri, E. S., Altucci, L., Amelio, I., Andrews, D. W., Annicchiarico-Petruzzelli, M., Antonov, A. V., Arama, E., Baehrecke, E. H., Barlev, N. A., Bazan, N. G., Bernassola, F., Bertrand, M. J. M., Bianchi, K., Blagosklonny, M. V., Blomgren, K., Borner, C., Boya, P., Brenner, C., Campanella, M., Candi, E., Carmona-Gutierrez, D., Cecconi, F., Chan, F. K., Chandel, N. S., Cheng, E. H., Chipuk, J. E., Cidlowski, J. A., Ciechanover, A., Cohen, G. M., Conrad, M., Cubillos-Ruiz, J. R., Czabotar, P. E., D'Angiolella, V., Dawson, T. M., Dawson, V. L., De Laurenzi, V., De Maria, R., Debatin, K. M., DeBerardinis, R. J., Deshmukh, M., Di Daniele, N., Di Virgilio, F., Dixit, V. M., Dixon, S. J., Duckett, C. S., Dynlacht, B. D., El-Deiry, W. S., Elrod, J. W., Fimia, G. M., Fulda, S., Garcia-Saez, A. J., Garg, A. D., Garrido, C., Gavathiotis, E., Golstein, P., Gottlieb, E., Green, D. R., Greene, L. A., Gronemeyer, H., Gross, A., Hajnoczky, G., Hardwick, J. M., Harris, I. S., Hengartner, M. O., Hetz, C., Ichijo, H., Jaattela, M., Joseph, B., Jost, P. J., Juin, P. P., Kaiser, W. J., Karin, M., Kaufmann, T., Kepp, O., Kimchi, A., Kitsis, R. N., Klionsky, D. J., Knight, R. A., Kumar, S., Lee, S. W., Lemasters, J. J., Levine, B., Linkermann, A., Lipton, S. A., Lockshin, R. A., Lopez-Otin, C., Lowe, S. W., Luedde, T., Lugli, E., MacFarlane, M., Madeo, F., Malewicz, M., Malorni, W., Manic, G., Marine, J. C., Martin, S. J., Martinou, J. C., Medema, J. P., Mehlen, P., Meier, P., Melino, S., Miao, E. A., Molkentin, J. D., Moll, U. M., Munoz-Pinedo, C., Nagata, S., Nunez, G., Oberst, A., Oren, M., Overholtzer, M., Pagano, M.,

Panaretakis, T., Pasparakis, M., Penninger, J. M., Pereira, D. M., Pervaiz, S., Peter, M. E., Piacentini, M., Pinton, P., Prehn, J. H. M., Puthalakath, H., Rabinovich, G. A., Rehm, M., Rizzuto, R., Rodrigues, C. M. P., Rubinsztein, D. C., Rudel, T., Ryan, K. M., Sayan, E., Scorrano, L., Shao, F., Shi, Y., Silke, J., Simon, H. U., Sistigu, A., Stockwell, B. R., Strasser, A., Szabadkai, G., Tait, S. W. G., Tang, D., Tavernarakis, N., Thorburn, A., Tsujimoto, Y., Turk, B., Vanden Berghe, T., Vandenabeele, P., Vander Heiden, M. G., Villunger, A., Virgin, H. W., Vousden, K. H., Vucic, D., Wagner, E. F., Walczak, H., Wallach, D., Wang, Y., Wells, J. A., Wood, W., Yuan, J., Zakeri, Z., Zhivotovsky, B., Zitvogel, L., Melino, G., and Kroemer, G. (2018) Molecular mechanisms of cell death: recommendations of the Nomenclature Committee on Cell Death 2018. *Cell Death Differ* **25**, 486-541

57. Acharjee, S., Verbeek, M., Gomez, C. D., Bisht, K., Lee, B., Benoit, L., Sharkey, K. A., Benediktsson, A., Tremblay, M. E., and Pittman, Q. J. (2018) Reduced Microglial Activity and Enhanced Glutamate Transmission in the Basolateral Amygdala in Early CNS Autoimmunity. *The Journal of neuroscience : the official journal of the Society for Neuroscience* **38**, 9019-9033
58. Marin-Teva, J. L., Dusart, I., Colin, C., Gervais, A., van Rooijen, N., and Mallat, M. (2004) Microglia promote the death of developing Purkinje cells. *Neuron* **41**, 535-547
59. Sedel, F., Bechade, C., Vyas, S., and Triller, A. (2004) Macrophage-derived tumor necrosis factor alpha, an early developmental signal for motoneuron death. *The Journal of neuroscience : the official journal of the Society for Neuroscience* **24**, 2236-2246
60. Cusack, C. L., Swahari, V., Hampton Henley, W., Michael Ramsey, J., and Deshmukh, M. (2013) Distinct pathways mediate axon degeneration during apoptosis and axon-specific pruning. *Nat Commun* **4**, 1876
61. Mattson, M. P., Keller, J. N., and Begley, J. G. (1998) Evidence for synaptic apoptosis. *Exp Neurol* **153**, 35-48
62. Nguyen, Q. T., Sanes, J. R., and Lichtman, J. W. (2002) Pre-existing pathways promote precise projection patterns. *Nature neuroscience* **5**, 861-867
63. Jiang, Y. Q., Zaaimi, B., and Martin, J. H. (2016) Competition with Primary Sensory Afferents Drives Remodeling of Corticospinal Axons in Mature Spinal Motor Circuits. *The Journal of neuroscience : the official journal of the Society for Neuroscience* **36**, 193-203
64. Syroid, D. E., Maycox, P. R., Burrola, P. G., Liu, N., Wen, D., Lee, K. F., Lemke, G., and Kilpatrick, T. J. (1996) Cell death in the Schwann cell lineage and its regulation by neuregulin. *Proc Natl Acad Sci U S A* **93**, 9229-9234

65. Nave, K. A., and Salzer, J. L. (2006) Axonal regulation of myelination by neuregulin 1. *Curr Opin Neurobiol* **16**, 492-500

66. Stassart, R. M., Fledrich, R., Velanac, V., Brinkmann, B. G., Schwab, M. H., Meijer, D., Sereda, M. W., and Nave, K. A. (2013) A role for Schwann cell-derived neuregulin-1 in remyelination. *Nature neuroscience* **16**, 48-54

67. Ngo, S. T., Cole, R. N., Sunn, N., Phillips, W. D., and Noakes, P. G. (2012) Neuregulin-1 potentiates agrin-induced acetylcholine receptor clustering through muscle-specific kinase phosphorylation. *Journal of cell science* **125**, 1531-1543

68. Orci, L., Ravazzola, M., Le Coadic, M., Shen, W. W., Demaurex, N., and Cosson, P. (2009) From the Cover: STIM1-induced precortical and cortical subdomains of the endoplasmic reticulum. *Proc Natl Acad Sci U S A* **106**, 19358-19362

69. Giordano, F., Saheki, Y., Idevall-Hagren, O., Colombo, S. F., Pirruccello, M., Milosevic, I., Gracheva, E. O., Bagriantsev, S. N., Borgese, N., and De Camilli, P. (2013) PI(4,5)P(2)-dependent and Ca(2+)-regulated ER-PM interactions mediated by the extended synaptotagmins. *Cell* **153**, 1494-1509

70. Misonou, H., Thompson, S. M., and Cai, X. (2008) Dynamic regulation of the Kv2.1 voltage-gated potassium channel during brain ischemia through neuroglial interaction. *Journal of Neuroscience* **28**, 8529-8538

71. Romer, S. H., Dominguez, K. M., Gelpi, M. W., Deardorff, A. S., Tracy, R. C., and Fyffe, R. E. (2014) Redistribution of Kv2.1 ion channels on spinal motoneurons following peripheral nerve injury. *Brain Res* **1547**, 1-15

72. Vullhorst, D., Mitchell, R. M., Keating, C., Roychowdhury, S., Karavanova, I., Tao-Cheng, J. H., and Buonanno, A. (2015) A negative feedback loop controls NMDA receptor function in cortical interneurons via neuregulin 2/ErbB4 signalling. *Nat Commun* **6**, 7222

73. Song, F., Chiang, P., Wang, J., Ravits, J., and Loeb, J. A. (2012) Aberrant neuregulin 1 signaling in amyotrophic lateral sclerosis. *J Neuropathol Exp Neurol* **71**, 104-115

74. Lasiene, J., Komine, O., Fujimori-Tonou, N., Powers, B., Endo, F., Watanabe, S., Shijie, J., Ravits, J., Horner, P., Misawa, H., and Yamanaka, K. (2016) Neuregulin 1 confers neuroprotection in SOD1-linked amyotrophic lateral sclerosis mice via restoration of C-boutons of spinal motor neurons. *Acta Neuropathol Commun* **4**, 15

75. Song, F., Chiang, P., Ravits, J., and Loeb, J. A. (2014) Activation of microglial neuregulin1 signaling in the corticospinal tracts of ALS patients with upper motor neuron signs. *Amyotroph Lateral Scler Frontotemporal Degener* **15**, 77-83

76. Mancuso, R., Martinez-Muriana, A., Leiva, T., Gregorio, D., Ariza, L., Morell, M., Esteban-Perez, J., Garcia-Redondo, A., Calvo, A. C., Atencia-Cibreiro, G., Corfas, G., Osta, R., Bosch, A., and Navarro, X. (2016) Neuregulin-1 promotes functional improvement by enhancing collateral sprouting in SOD1(G93A) ALS mice and after partial muscle denervation. *Neurobiol Dis* **95**, 168-178

Figure legends

Figure 1. C-boutons on normal spinal cord MNs (visualized by Nissl staining, blue) after double fluorescent immunolabeling. **a)** A MN soma showing the concentration of M2 AChR (green) in close apposition with VAChT-labeled synaptic terminals (red); in the enlarged insets the displacement of the presynaptic VAChT-signal with respect to the postsynaptic M2 AChR labeling can be seen. **b)** MN soma showing the close relationship of S1R (green) with VAChT-labeled synaptic terminals (red); note in the insets the displacement of S1R signal respect to VAChT reflecting the postsynaptic localization of S1R; S1R is also present on MN soma in non-synaptically associated particles (encircled), which presumably correspond to ER stacks. **c)** A MN soma showing the association between NRG1 patches (green) with VAChT-labeled synaptic terminals (red); in the enlarged insets the displacement of the presynaptic VAChT-signal with respect to the postsynaptic NRG1 labeling can be observed. **d)** A MN soma showing that clusters of NRG1 (green) co-localize with Kv2.1 potassium channels (red) at C-bouton sites; in the enlarged insets the co-localizing signal is seen in yellow. **e)** A MN somata showing the co-localization between p-ErbB2 (green) and most of the VAChT-labeled synaptic terminals (red); the enlarged insets show a detail of two VAChT-positive terminals (red), one of them colocalizing with p-ErbB2 immunolabeling (yellow). Scale bars: 10 µm in **e** (valid for **a-d**).

Figure 2. Ultrastructure of C-bouton synaptic terminals. **a)** A presynaptic terminal (colored green) apposed to the surface of a MN cell body (colored red) displaying a SSC (delimited by arrows). **b)** A coated endocytic vesicle located at the periphery of the terminal in **(a)** (delimited by the dotted circle) is shown. **c)** A detail of a presumably endocytic/autophagic structure (*) within the nerve terminal is shown. **d)** A detail of compartmentation of pre- and postsynaptic elements in C-bouton is shown; the extracellular space (yellow) is interposed between the presynaptic terminal (green) and the postsynaptic MN cell body (red); the postsynaptic membrane displays an intimately associated SSC (blue) that exhibits continuity with ER membranes at the MN cell body (arrow). Scale bars: 250 nm.

Figure 3. Disruption of NRG1 clusters at C-boutons in acutely stressed MNs. **a-e)** Lumbar spinal cord MNs were antidromically stimulated by electrical pulses delivered through sciatic nerve (5V, 10 Hz, 60 min). Double immunolabeling for NRG1 (green) and VAChT (blue) shows an important disruption of NRG1 clusters in stimulated MNs (**c,d**) versus those in the control side (**a,b**). Densitometric measurements of NRG1 labeling at VAChT-positive C-bouton sites shows the presence of a NRG1-depleted population of cholinergic synapses **(e)**. **f-k)** MNs in lumbar

spinal cords were subjected to orthodromic electrical field stimulation (5V, 10 Hz, 30 min). Double immunolabeling for NRG1 (green) and VAChT (blue) shows an important depletion of NRG1 in stimulated MNs (**h,i**) versus control ones (**f,g**). **j)** Ultrastructural morphology of C-bouton area from a stimulated MN shows a disrupted SSC (arrows and colored blue in the inset), and the accumulation of large vesicles and vacuoles (red * in the inset), presumably representing disorganized ER at the cortical areas (delimited by double arrows) of the MN; presynaptic terminals are colored green, whereas postsynaptic MN is colored red; ER stacks in the deeper regions of MN soma appear not altered (yellow *). **k)** Densitometric analysis of VAChT and NRG1 in individual C-boutons demonstrates the huge depletion of NRG1 after stimulation. **l-t)** Effects of acute spinal cord slicing on C-bouton organization; MN cell bodies double immunolabeled for NRG1 (green) and VAChT (blue) in a spinal cord slice from a whole body PF-perfused mouse used as control (**l,m**) and in a sample obtained from an acute spinal cord oxygenated in artificial LCR and subsequently fixed by immersion in PF for 10 min (**n,q**). Note the dispersion and fragmentation of NRG1 clusters after slicing in conjunction with a depletion of VAChT-positive puncta **(n,o)** or the near complete depletion of NRG1 clusters **(p,q)**. **r,s)** Semithin plastic sections of a control-fixed MN (**r**) and a MN fixed after 10 min of slicing (**s**) showing the cytoplasmic microvacuolization induced by the slicing process. **t)** The quantification of NRG1 cluster size (in μm^2) shows its reduction after slicing, which is not prevented when a 0 Ca^{2+} medium is used. Values in graphs are shown as mean ± SEM; ***p < 0.001 (Student's *t*-test [e and k] and one way ANOVA, Bonferroni's post-hoc test [t]); n in e = 184, contralateral and 219, ipsilateral; n in k = 117, cont. and 53, stim., and n in t = 42-151. Scale bar: 500 nm in **j** (250 nm in inset); 20 µm in **q** (valid for **a-d**; **f-l** and **l-p**); 10 µm in **s** (valid for **r**).

Figure 4. Correlative changes in MN cell bodies, glial cells and NRG1 clusters, and VAChT-positive C-bouton synaptic sites after axotomy (either peripheral nerve irreversible transection or crush); only data from long-term (120-180 days) crush experiments allowing permissive reinnervation are shown. **a)** Measurements of MN soma size (*p < 0.05 and ***p < 0.001 vs. 0 day, or crush vs. respective transection time point), one-way ANOVA, Bonferoni's post-hoc test); n = 14-52 MNs from 2-4 animals. **b)** Time course of microglial and astroglial activation around axotomyzed MNs; *p < 0.05 and ***p < 0.001 vs. 0 day, or crush vs. respective transection time point (two-way ANOVA, Bonferroni's post-hoc test); n = 5-25 sections from 2-4 animals. **c, d)** Time course of density (**c**) and size (**d**) of VAChT- and NRG1-labeled C-boutons in axotomyzed MNs; *p < 0.05, **p < 0.01 and ***p < 0.001 vs. respective time-point of VAChT after axotomy, or crush vs. respective transection time point (two-way ANOVA, Bonferroni's

post-hoc test); n = in **c** = 10-52 and in **d** = 25-180 MNs, from 2-4 animals. **e-h)** Microglial reaction adjacent to MN cell bodies in the axotomized (ipsi) side (7 days after lesion) **(f, g)** compared to the unoperated (contra) side **(e)**; MN cell bodies are delimited by Nissl staining (blue), C-bouton sites and microglia are visualized by NRG1 (green) and Iba1 (red) immunolabeling, respectively; note the prominent microglial recruitment seen around axotomyzed MN cell bodies (**f, g**). A detail of the spatial relation between microglial processes (Iba1, red) and clustered NRG1 (green) at C-bouton after a 3D reconstruction is shown in **h**. **i)** Number of NRG1-positive spots interacting with microglial processes; note their rapid reduction 24 h after axotomy, indicating that C-boutons are disrupted following the initial and rapid microglial recruitment; *p < 0.05 and ***p < 0.001 vs. 0 days (one-way ANOVA, Bonferroni's post-hoc test); n = 10-21 3D reconstructed MNs. **j-k)** Interaction between microglial processes and C-bouton sites in 14 days-axotomyzed MNs; **j)** shows MN cell bodies (delimited by dashed lines) exhibiting microglial recruitment (Iba1, red) in relation with VAChT- (blue) and NRG1- (green) labeled puncta; note that the NRG1 spots, which are more intimately in contact with microglial processes, are devoid of VAChT immunolabeling (see the insets), suggesting that they correspond to denervated C-bouton sites; this aspect is quantified in **k,** showing the ratio between NRG1 and VAChT immunoreactivity in spots associated or not with Iba1 microglial profiles; note that postsynaptic NRG1 positive clusters still persisted in sites in which presynaptic VAChT is already removed by microglia. **p < 0.01 (Student's t-test); n = 27 clusters in the 2 3D reconstructed MNs showed in **j.** Data in graphs are shown as mean ± SEM. Scale bars: 50 μm in **f** (valid for e); 20 μm in **g**; 5 μm in **h**; 20 μm in **j**.

Figure 5. Ultrastructural alterations of MN afferent synapses in concomitance with microglial recruitment at the surface of MN somata 7days after peripheral nerve transection. **a-b)** Semithin plastic sections of control (**a**) and axotomyzed (**b**) MN somata; note the recruitment of microglial cells (arrows), some of them, in close contact with the MN cell body surface of the injured MN. **c-e)** Electron micrographs of cell bodies and dendrites (colored red) of unaxotomized MNs showing abundant afferent synaptic boutons (colored violet and indicated with *); normal C-type synapses are shown in (**d** and **e**); observe that presynaptic terminals filled with synaptic vesicles are in front of the postsynaptic membrane which is in close association with SSC (arrows in **d,** and colored blue in **d** and **e**); the extracellular space, interposed between pre- and postsynaptic structures, was marked in yellow in **d** and **e**. **f-l)** Ultrastructural morphology of an axotomyzed MN cell body (colored red) in contact with recruited microglial cell (colored green); a degenerating dark terminal synaptic bouton is interposed between both cells (*); a portion of MN surface containing a presumably

denervated SSC is seen contacting a microglial cell (delimited by a rectangle and enlarged in **g**). Another example of degenerating synaptic bouton (*), interposed between a recruited microglial cell (colored green) and an axotomyzed MN soma (dashed in red) is shown in (**h**). **i-k)** A recruited microglial cell (colored green) over a denervated postsynaptic site of a C-boutonon an axotomyzed MN (colored red) is shown in **i**; this postsynaptic locus was formerly occupied by a presynaptic terminal which, once removed, its adjacent postsynaptic SSC structure remains as an indicator of the denervated C-bouton site; the relationship between these compartments are depicted in **j** and **k** as follows: MN soma red; microglia, green; SSC, blue; and extracellular space, yellow. Scale bars: 10 μm in **b** (valid for **a**), 500 nm in **c** and **d,** 200 nm in **e**, 1 μm in **f** and **h**, 2.5 μm in **I**, and 200 nm in **h**.

Figure 6. Animals were treated with vehicle or the ER-stress inhibitor salubrinal, subjected to sciatic nerve transection and examined 7 days later. **a-f)** The axotomyzed MN pool was analyzed by double immunofluorescent staining for BiP (green) and Iba1 (red). **g-l)** The same samples were labeled for Nissl (blue), NRG1 (green), VAChT (blue) and Iba1 (red). **m-p)** Quantitative analysis of changes in BiP-immunostaining intensity (**m**), microglial covering of MN soma perimeter (**n**) and density of VAChT- and NRG1-positive spots (per 100 μm^2) (**o** and **p**, respectively); note that the treatment with salubrinal significantly reverts the BiP upregulation, microglial activation and C-bouton loss that occurs in/or adjacent to axotomyzed MNs; Data are shown as mean ± SEM. ***$p < 0.001$ vs. vehicle (Student's *t*-test), n (vehicle and salubrinal, respectively) = 203 and 179 MNs (in **m**); 41 and 66 MNs (in **n**); 22 and 47 MNs (in **o** and **p**), from 3 animals. Scale bars: 40 μm in **f** (valid for **a-e**) and 10 μm in **l** (valid for **g-k**).

Figure 7. Impact of the overexpression of different NRG1 isoforms in C-boutons on spinal cord MNs. **a)** Multiple fluorescent analysis of C-bouton-associated proteins in adult transgenic mice overexpressing HA-tag labeled NRG1 type III. The distribution of HA tag (red) NRG1 (visualized with an anti-pan-NRG1 antibody, green), and VAChT (blue) was detected in a Nissl-delimited MN cell body (gray); HA immunostaining exactly matches the anti-pan NRG1 signal and shows an extensive labeling along the whole MN surface; the VAChT-delimited C-bouton presynaptic sites display also association with NRG1, as detailed in the inset. **b)** The expression S1R, a protein focally concentrated in normal C-bouton SSCs, is largely expanded along the MN surface in NRG1 type III overexpressors: the extensive surface labeling of HA tag (red) and NRG1 (green) is associated with wide S1R immunostaining (blue). However, whereas there was an exact colocalization between HA and NRG1, sites containing S1R belong to separate microdomains, as evidenced after the plot profile analysis of fluorescence intensity depicted in

c and **d**. **e)** The enlarged expression of NRG1 (green) at the MN surface is associated with the expansion of the SSC marker Kv2.1 (red); both signals are largely co-localized (yellow, in merge panel, and white, after co-localization analysis, Person´s R = 0.67). **f)** Show the altered distribution of M2 muscarinic AChRs in the NRG1 type III overexpressors. The extensive surface immunolabeling of M2 AChRs (green) exceeds the area corresponding to VAChT-labeled cholinergic terminals (red), as seen detailed in the inset. **g)** Multiple immunofluorescent analysis of C-boutons on a spinal cord MN from a transgenic mouse overexpressing HA-NRG1-GIEF, a BACE1-cleaved variant of NRG1 type III [36]. The Nissl-delimitated MN cell body (gray) displays abundant HA-tag signal inside the MN cytoplasm and adjacent dendrites (red); HA-tag signal does not colocalize with either the NGR1, when detected with an anti-pan-NRG1 antibody, (green), or VAChT-positive terminals (blue); however, C-bouton sites displaying VAChT puncta associated with postsynaptic NRG1, do not contain HA-positive signal, indicating the absence of BACE1-processed NRG1 type III (insets). The white granules in the merge image are lipofuscin particles emitting unspecific fluorescence visible in the three channels. **h,i)** Multiple fluorescent analysis of C-bouton-associated proteins in adult transgenic mice overexpressing NRG1 type I; **h)** A MN, visualized after Nissl staining (gray), the anti-pan-NRG1 antibody (green) shows an extensive surface-associated immunolabeling; abundant C-bouton sites are visualized by S1R (red) and VAChT (blue) immunolabeling; NRG1 labeling at the MN surface exceeds out of the VAChT and S1R-containing synaptic sites (insets); **i)** A MN delimited by Nissl (gray) was immunolabeled for M2 AChR (green) and VAChT (red), showing the extensive surface expression of postsynaptic M2 AChR (inset). Both the number and size of C-boutons were dramatically increased, in NRG1 type I overexpressors. Scale bars: 10 μm in **i** (valid for **a**-**h**).

Figure 8. Quantification of C-bouton-associated markers in WT and transgenic mice overexpressing either NRG! type I or type III as indicated. The number and size of C-boutons in NRG1 type III overexpressors are not different from those in WT animals. However, in NRG1 type I overexpressors, both the number and size of C-boutons are dramatically increased. The postsynaptic expression of M2 AChRs, S1R and Kv2.1 are also largely increased in type III NRG1 overexpressors, whereas in NRG1 type I animals only M2 AChRs significantly increased. In all graphs values are shown as mean ± SEM; ***$p < 0.001$ (one-way ANOVA, Bonferroni's post-hoc test); n (WT, NRG1 type I and NRG1 type III , respectively) = 13, 13, and 9 MNs (in **a**); 92, 88, and 44 MNs (in **b**); 11, 10, and 13 MNs (in **c**); 8, 17 and 10 (in **d**), 5, 10 and 7 MNs (in **e**) from 2-3 animals per condition.

Figure 9. a-b) Electron micrographs of the cell body MN surface in transgenic mice overexpressing either NRG1 type III (**a**) or type I (**b**) isoforms. MN cytoplasm is dashed in red and C-bouton presynaptic terminals are marked in green. **a)** In NRG type III transgenic MNs, presynaptic terminals (*) are normal in size and located in face of enlarged and reduplicated SSC-like membranes (red arrows and bottom inset) in the postsynaptic MN; SSC-like membranes are extended far away from C-bouton sites. **b)** In NRG1 type I transgenic MNs the C-bouton presynaptic terminal (*) is highly enlarged and extends on the MN surface far away from the SSC-delimited area (colored blue) and detailed in the inset. **c)** The proposed changes in the structural and molecular organization of C-bouton synaptic sites, induced by overexpression of either NRG1 type III or type I isoforms, are depicted and compared to WT. Scale bar: 500 nm in **b** (valid for **a**).

Target	Source	Host species	Used concentration
Grp78 (BiP)	Stressgene (SPA-826), San Diego, CA, USA	Rabbit polyclonal	1:1000
Choline acetyltransferase (ChAT)	Millipore (AB144), Darmstadt, Germany	Goat polyclonal	1:250
Glial fibrillary acidic protein (GFAP)	Abcam (ab4674), Cambridge, UK	Chicken polyclonal	1:1000
Her4/ErbB4	Cell Signalling (#4795) Danvers, MA, USA	Rabbit monoclonal	1:50
HA Tag	Roche Diagnostics (11 867 423 001), Sant Cugat del Vallès, Barcelona	Rat monoclonal	1:500
Ionised calcium-binding adaptor molecule 1 (IBA1)	Abcam (ab5076)	Goat polyclonal	1:500
Kv2.1 α-subunit	NeuroMab (73-014), Davis, CA, USA	Mouse monoclonal	1:100
M2 muscarinic receptor	Alomone Labs (AMR-002), Jerusalem, Israel	Rabbit polyclonal	1:100
Neu (C-18) (ErbB2)	Santa Cruz Biotechnology (Sc-284), Dallas, TX, USA	Rabbit polyclonal	1:50
Neu/N	Chemicon International (MAB377), Temecula, CA, USA	Mouse monoclonal	1:100
NRG1 1α /β 1/2	Santa Cruz (sc-348)	Rabbit polyclonal	1:300
Neuregulin-1 Type III (extracellular)	Alomone labs (ANR-113)	Rabbit polyclonal	1:250
Neuregulin-CRD, Type III, clone N126B/31	Millipore (MABN534)	Mouse Monoclonal	1:250
p-Neu tyr1248 (p-ErbB2)	Santa Cruz (sc-293110)	Rabbit polyclonal	1:100
Sigma-1 receptor (S1R)	Santa Cruz (sc-137075)	Mouse monoclonal	1:50
SV2	Hybridoma bank (SV2), Iowa City, IA, USA	Mouse monoclonal	1:1000
Vesicular acetylcholine transporter (VAChT)	Synaptic Systems (139 105), Goettingen, Germany	Guinea pig polyclonal	1:500

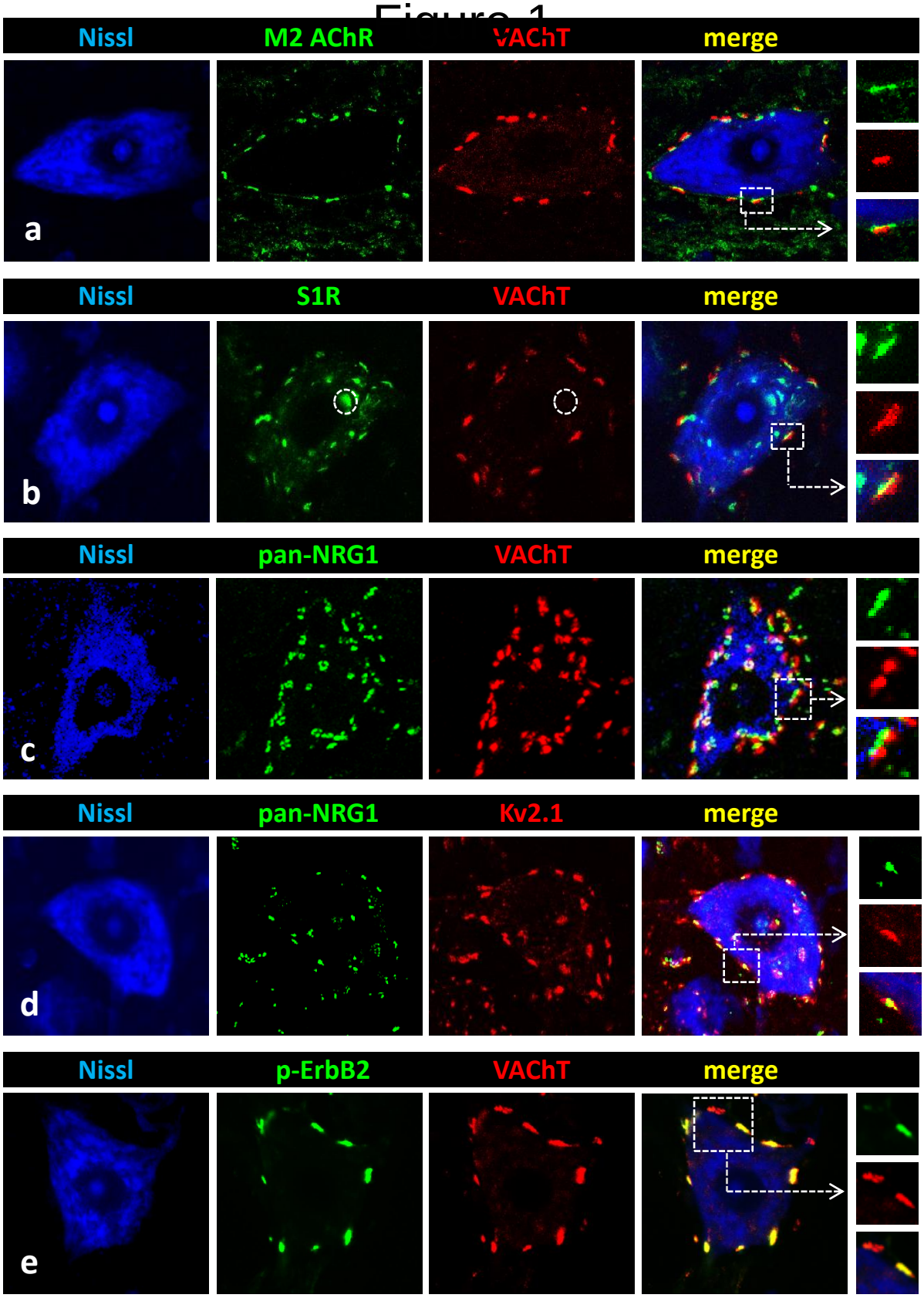
Nissl
M2 AChR
VAChT
merge
a
Nissl
S1R
VAChT
merge
b
Nissl
pan-NRG1
VAChT
merge
c
Nissl
pan-NRG1
Kv2.1
merge
d
Nissl
p-ErbB2
VAChT
merge
e

Figure 1

Figure 2

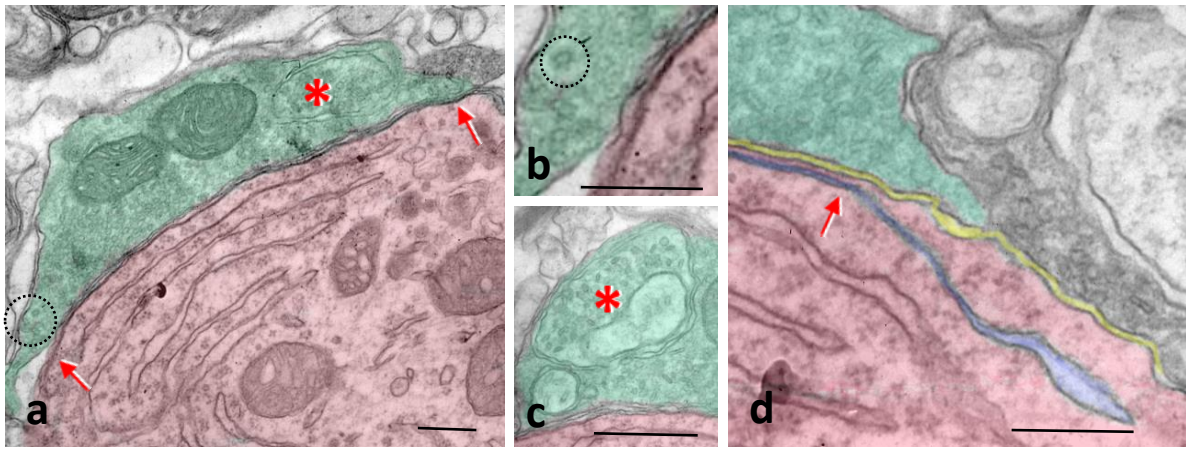

Figure 2

Figure 3

Antidromic stimulation

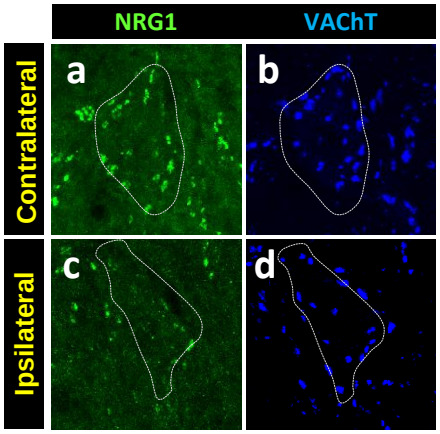

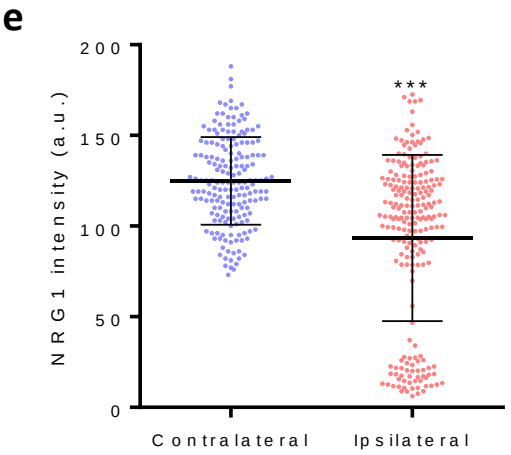

Orthodromic stimulation

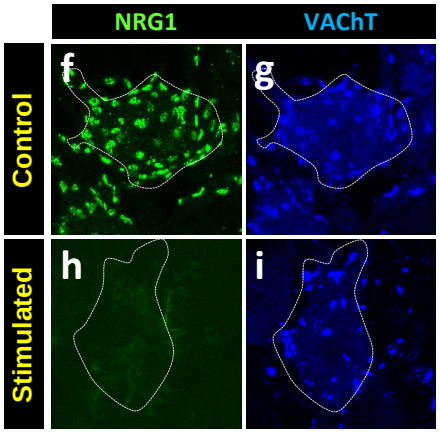

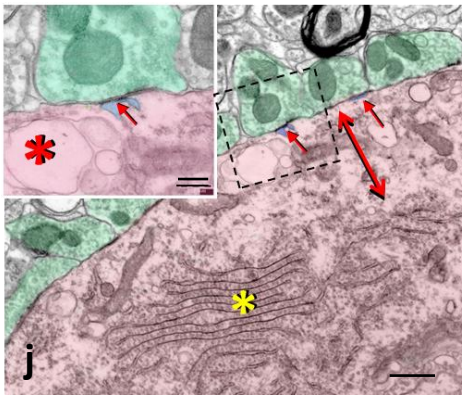

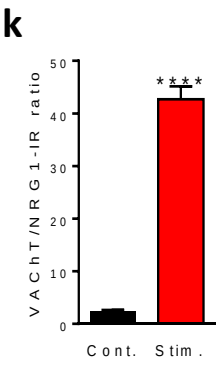

Ex vivo slice

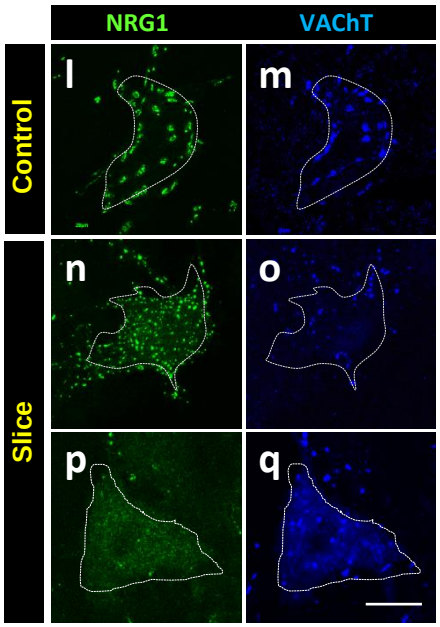

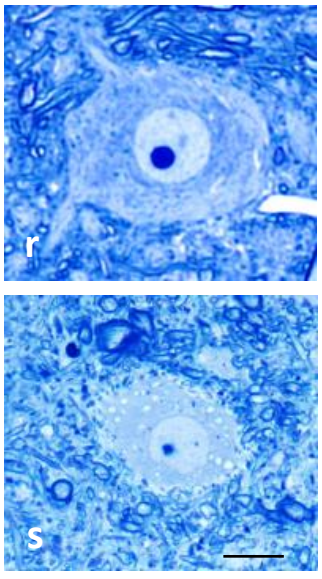

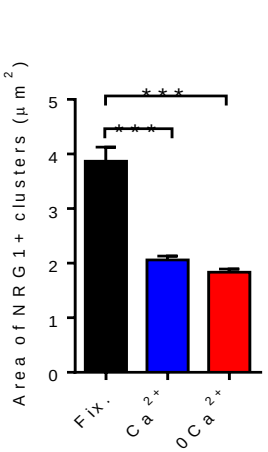

Figure 3

Figure 4

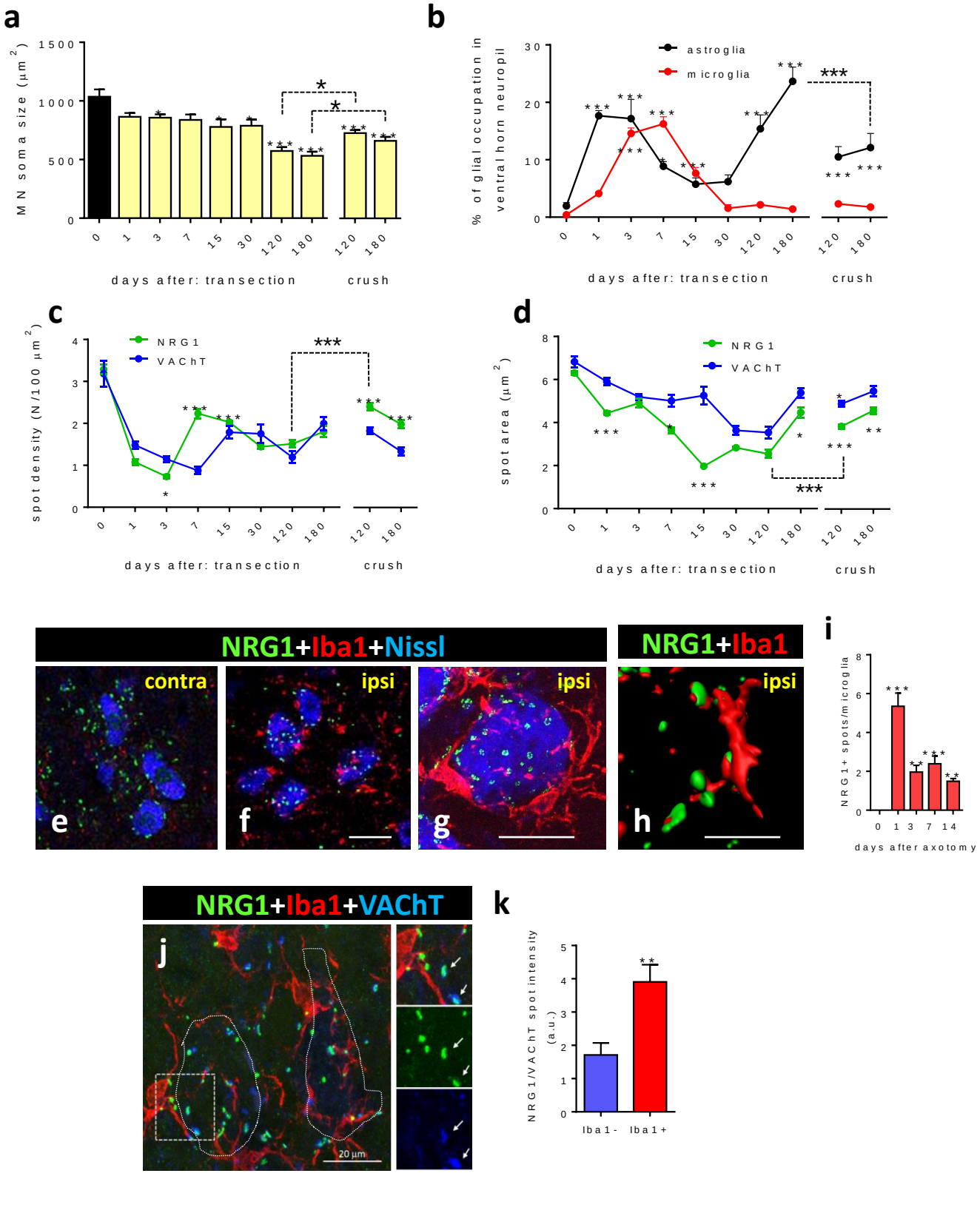

Figure 4

Figure 5

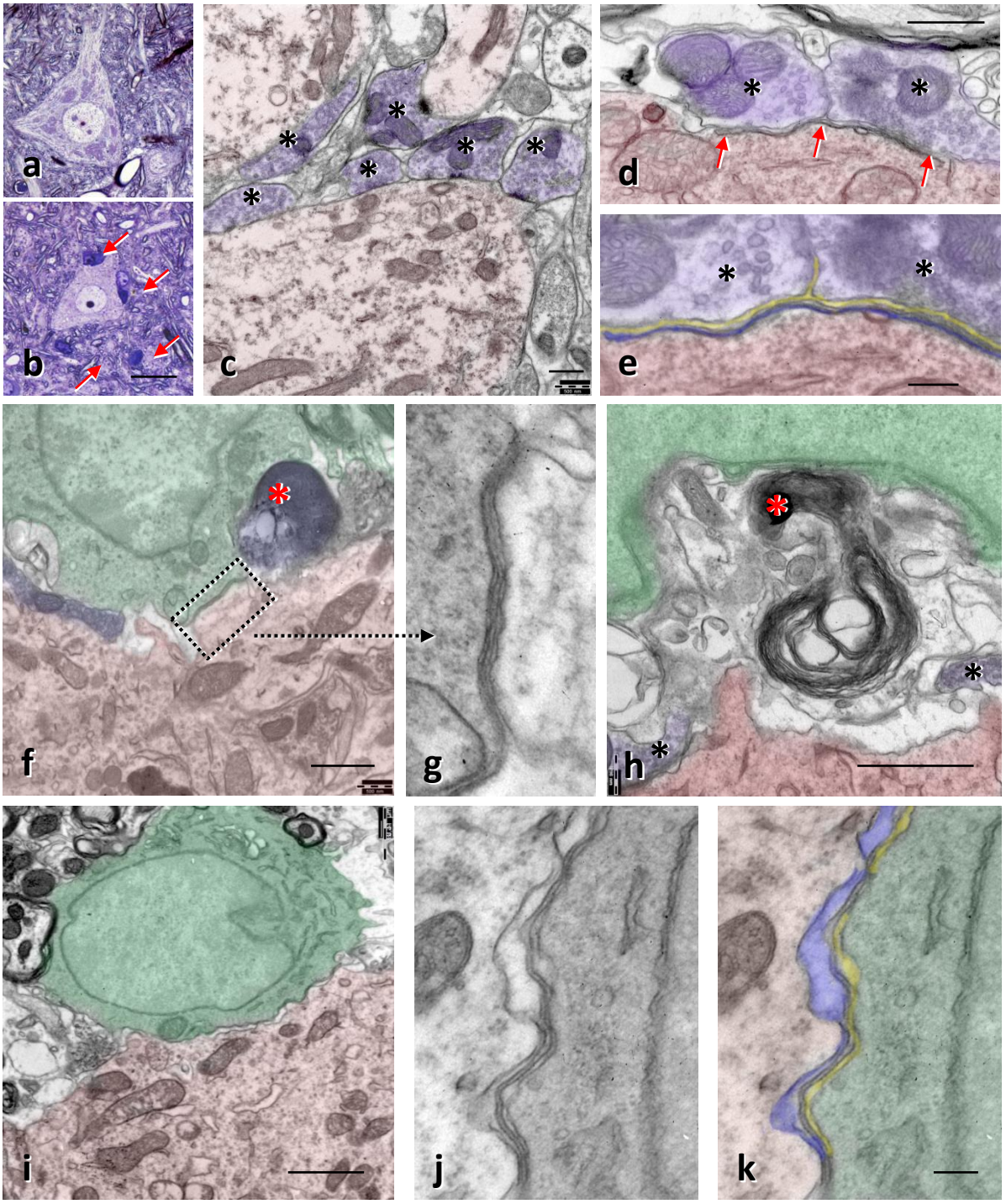

Figure 5

Figure 6

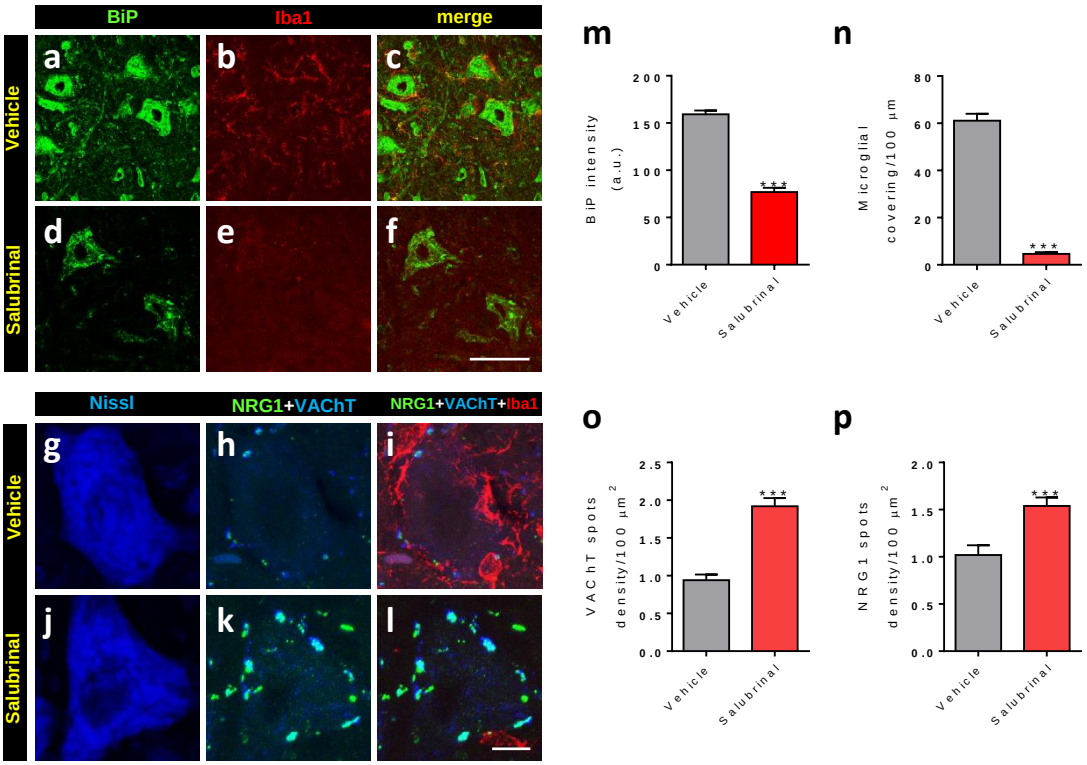

Figure 6

Figure 7

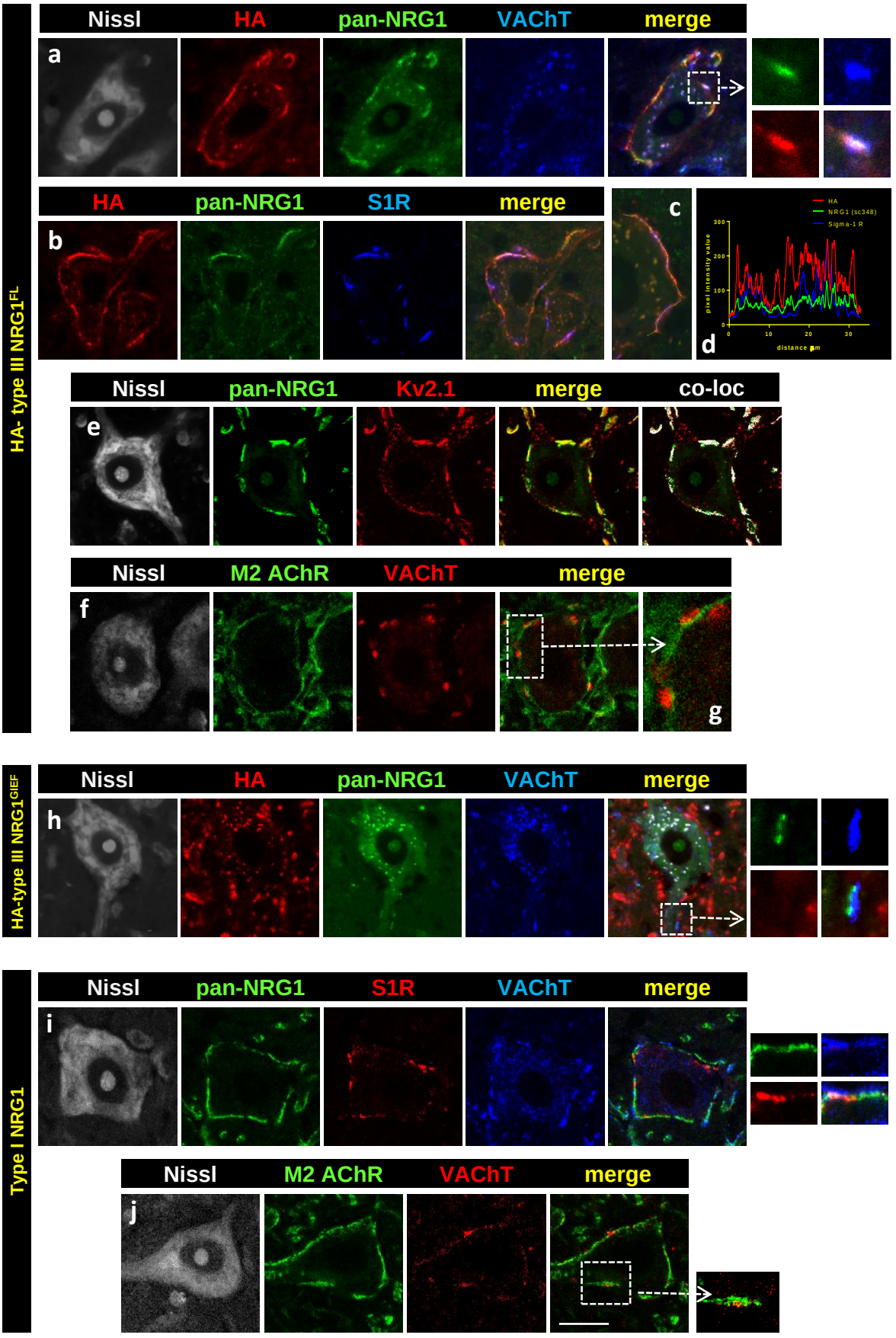

Figure 7

Figure 8

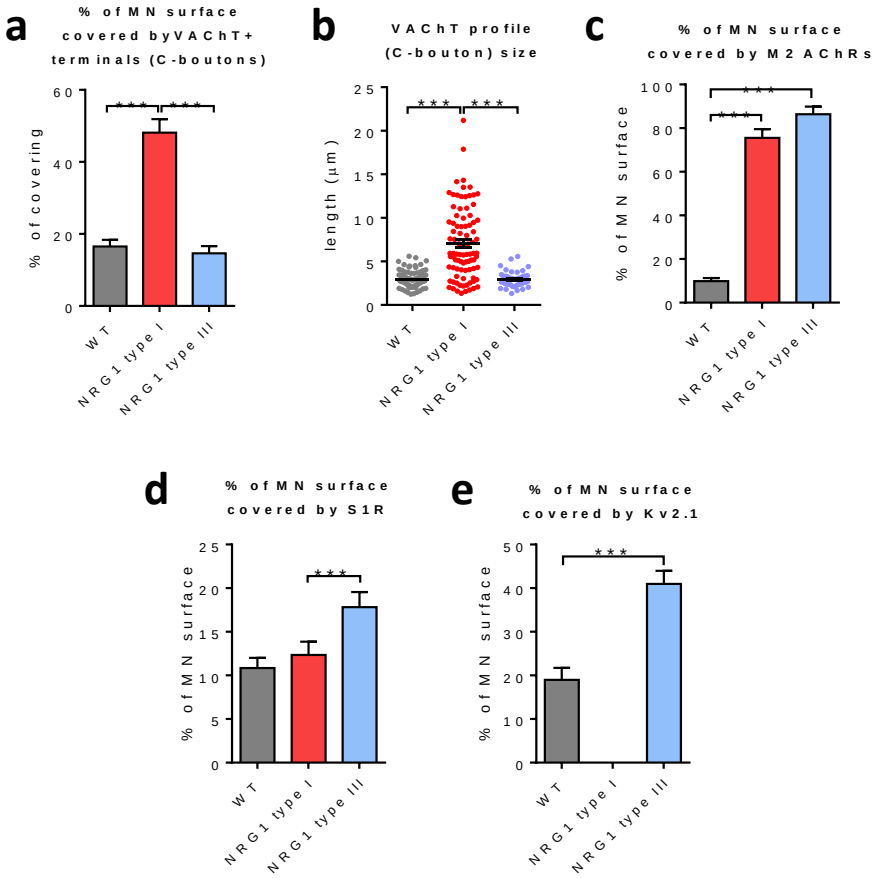

Figure 8

Figure 9

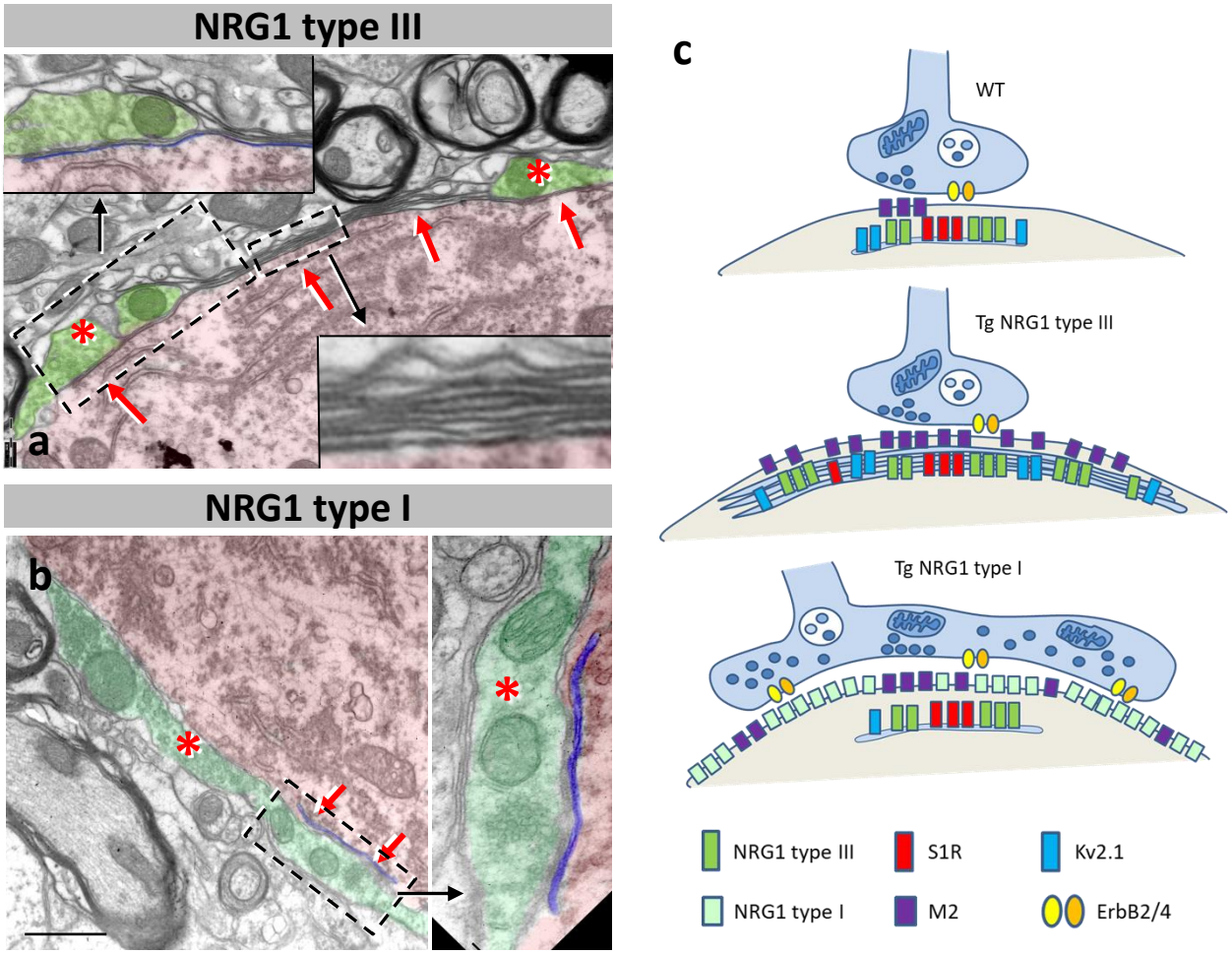

Figure 9

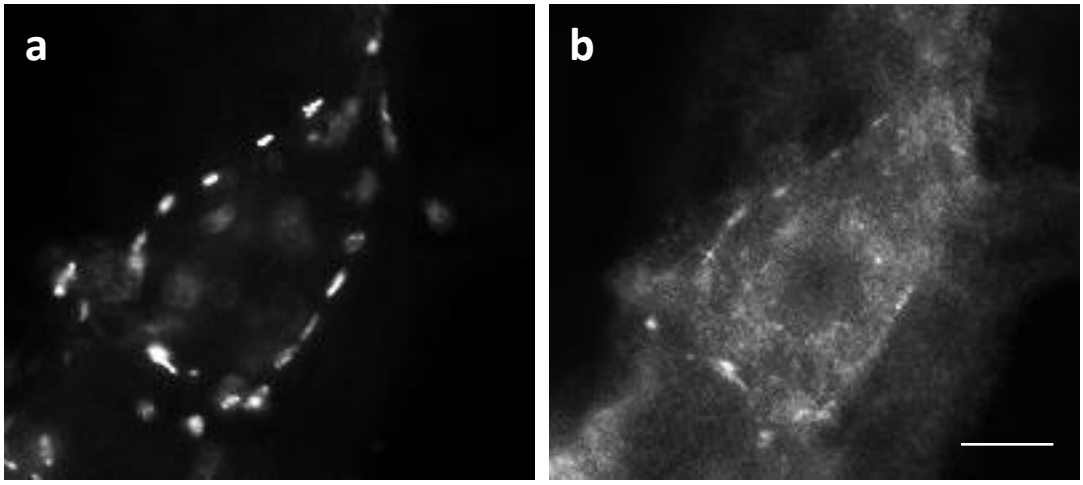

Neuregulin-1α/β1/2 (C-20)
sc-348
Santa Cruz, 1:200

Neuregulin-CRD, Type III
MABN534
Millipore, 1:250

Supplementary Figure 1. a and **b)** Spinal cord MN somata showing NRG1 immunoreactivity obtained by the two indicated antibodies simultaneously used. Note that both antibodies detect clusters of NRG1 representing C-bouton synaptic sites. However, the rabbit pan-anti-NRG1 antibody sc-348 displays more intense and clean immunolabeling than the mouse monoclonal MABN534, which is directed against type III NRG1-CRD. Scale bar: 10 µm in **b** (valid for **a**).

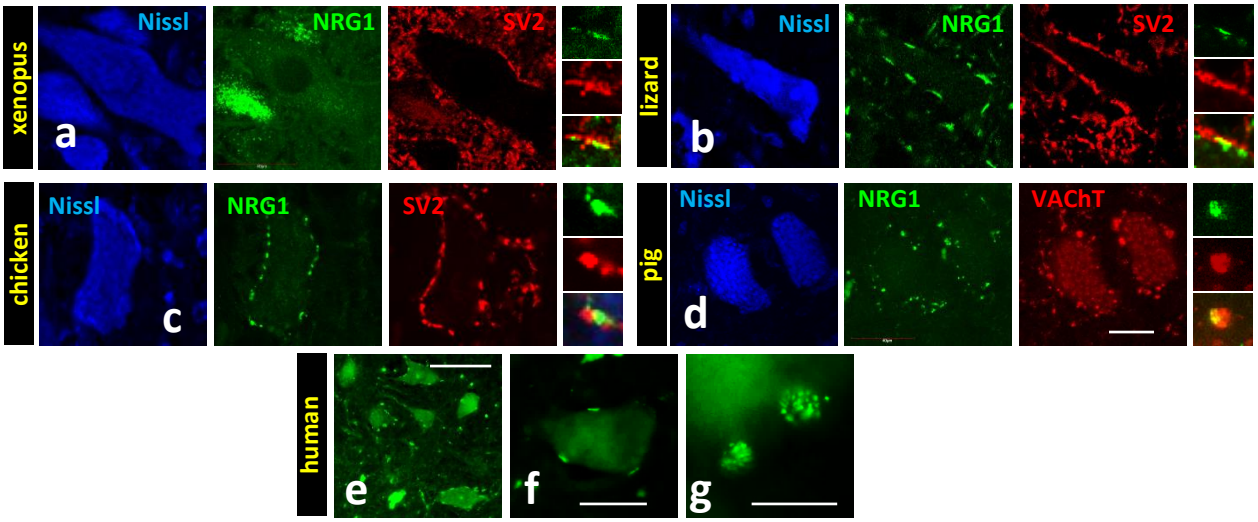

Supplementary Figure 2. Clusters of NRG1 are present in association with MN synaptic afferents in distinct indicated animal species. As anti-VAChT antibodies were not reactive in species different from mammals, synaptic sites were labeled with anti-SV2 antibodies in xenopus **(a)**, lizard **(b)** and chicken **(c)** samples; in pig samples **(d)** C-boutons were labeled with anti-VAChT antibodies, in human tissues **(e-g)**, NRG1-positive spots were seen adjacent to MN surface, in an identical pattern as observed in mice. MN cell bodies were delimited with fluorescent Nissl staining (blue). Scale bars: 20 µm in **d** (valid for **a-c**), 100 µm in **e**, 20 µm in **f** and 10 µm in **g**.

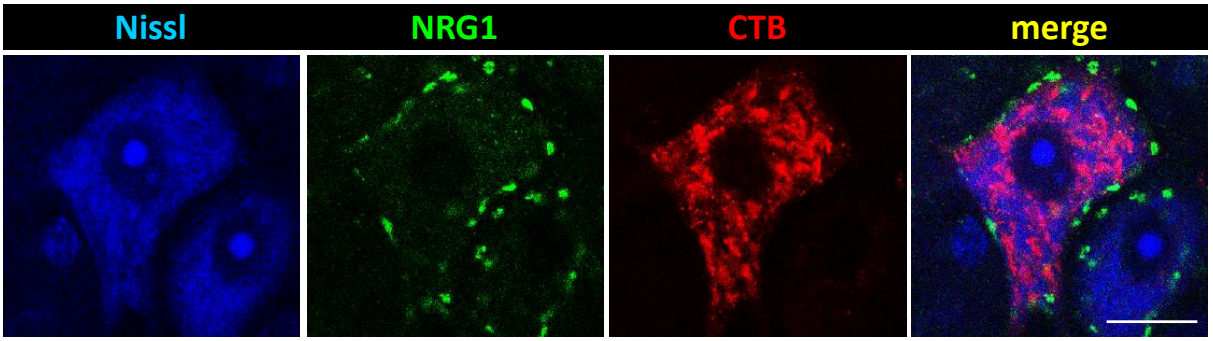

Supplementary Figure 3. Spinal cord MN somata, retrograde labeled by intramuscular injection of fluorescent CTB (red) was immunostained with anti-NRG1 antibody (green) and counterstained with Nissl (blue). Note that the extensive incorporation of CTB in MN cytoplasm does not overlap with NRG1 clustered at C-bouton sites. Scale bar: 20 µm.

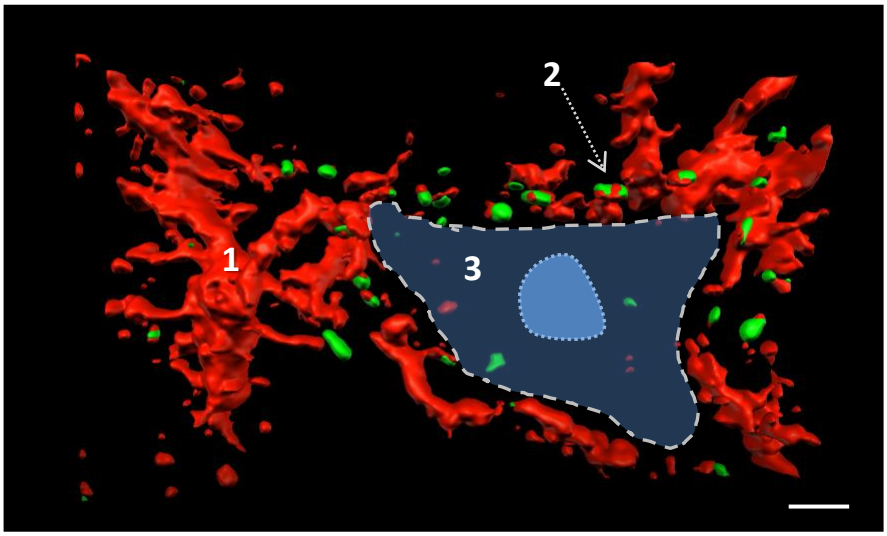

Supplementary Figure 4. 3D volume rendering displaying the close relationship between microglial processes and C-bouton associated NRG1 clusters. Image was obtained from stacked 0.5 µm optical confocal sections. A massive recruitment of microglia (red, 1) is seen around the MN soma (depicted, 3) 24 h after sciatic nerve axotomy. Microglial cells intimately interact with NRG1 clusters (green, 2). Scale bar: 5 µm.

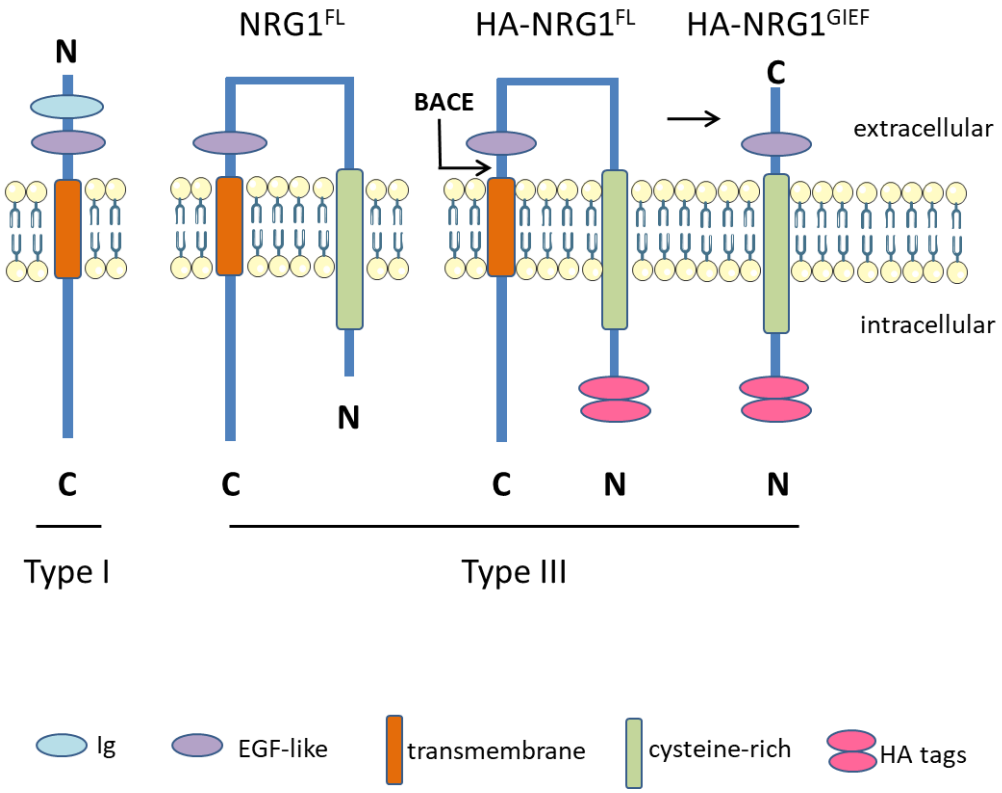

Supplementary Figure 5. Membrane disposition of NRG1 isoforms (adapted from [36,65]).

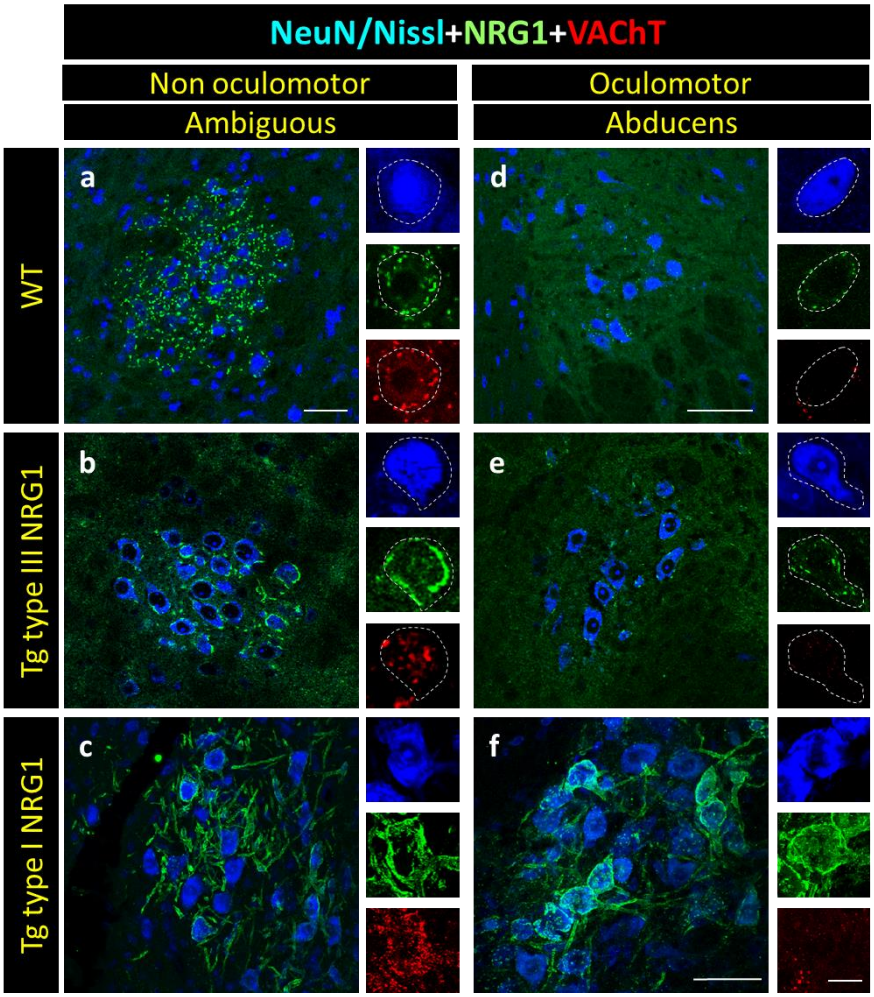

Supplementary Figure 6. Impact of NRG1 overexpression in C-bouton organization of brainstem (non-oculomotor [non-OCM, **a**, **b** and **c**] and oculomotor [OCM, **d**, **e** and **f**]) MNs. Selected sections were triple fluorescent labeled with NRG1 (green), VAChT (red) and MN cell bodies were delimited by either Nissl (**a**, and **d**) or NeuN (**b**, **c, e** and **f**) staining (blue). **a)** Non-OCM (ambiguous, cranial nerve [CN] X) MNs display NRG1 clusters associated with VAChT positive terminals, in an identical pattern to that observed in ventral horn spinal cord MNs. **b** and **c)** In samples from transgenic mice overexpressing either NRG1 type III or NRG1 type I, the observed changes are the same as those observed for ventral horn spinal cord MNs: the expanded superficial expression of postsynaptic NRG1 is detected in both models (green in **b** and **c**), whereas an important increase in the number of cholinergic VAChT positive terminals is noticed in NRG1 type I overexpressors (red in **c**). Identical results were observed in other brainstem non-OCM MN nuclei, such as: facial (CNVII), motor trigeminal (CNV) and hypoglosus (CNXII) (not shown). **d)** WT OCM (abducens, CNVI) MNs are devoid of VAChT positive C-bouton afferents, and clusters of NRG1 are scarce and not associated to cholinergic synapses. **e)** After overexpression of NRG1 type III, an increase in NRG1 clusters in OCM MN somata, which are non-associated to VAChT-positive terminals, are noticed. **f)** After NRG1 type I overexpression a dramatic increase in surface associated NRG1 in OCM MNs are detected, however, contrasting to that found in non-OCM MNs, excess of NRG1 is not able to induce cholinergic (VAChT-positive) synaptogenesis. Scale bars: 50 µm in **a**, **d** and **f** (valid for **b**, **c** and **e**), 10 µm in the inset in **f** (valid for all insets).